Four-dimensional Variability of Composite Halokinetic Sequences

*Leonardo Muniz Pichel, Christopher A-L. Jackson

Basins Research Group (BRG), Department of Earth Science and Engineering, Imperial College London, South Kensington Campus, SW7 2BP, United Kingdom

*email: l.muniz-pereira@imperial.ac.uk

ABSTRACT

The architecture of salt diapir-flank strata (i.e. halokinetic sequences) is controlled by the interplay between volumetric diapiric flux and sediment accumulation. Halokinetic sequences consist of unconformity-bounded packages of thinned and folded strata formed by drape-folding around passive diapirs. They are described by two end-members: (i) *hooks*, which are characterized by narrow zones of folding (<200 m) and high taper angles (>70°); and (ii) *wedges*, typified by broad zones of folding (300-1000 m) and low taper angles (<30°). Hooks and wedges stack to form tabular and tapered composite halokinetic sequences (CHS), respectively. CHSs were most thoroughly described from outcrop-based studies that, although able to capture their high-resolution facies variations, are limited in describing their 4D variability. This study integrates 3D seismic data from the Precaspian Basin and restorations to examine variations in CHS architecture through time and space along diapirs with variable plan-form and cross-sectional geometries. The diapirs consist of curvilinear walls that vary from upright to inclined and locally display well-developed salt shoulders and/or laterally transition into rollers. CHS are highly variable in both time and space, even along a single diapir or minibasin. A single CHS can transition along a salt wall from tabular to tapered geometries. They can be downturned and exhibit rollover-synclinal geometries with thickening towards the diapir above salt shoulders. Inclined walls present a greater proportion of tapered CHSs implying an overall greater ratio between sediment accumulation and salt-rise relatively to vertical walls. In terms of vertical stacking, CHS can present a typical zonation with lower tapered, intermediate tabular and upper tapered CHSs, but also unique patterns where the lower sequences are tabular and transition upward to tapered CHS. The study demonstrates that CHSs are more variable than previously documented, indicating a complex interplay between volumetric salt rise, diapir-flank geometry, sediment accumulation and roof dimensions.

1. INTRODUCTION

Salt diapirism and the associated development of minibasins are fundamental processes in salt-rich sedimentary basins. Salt diapirs can rise in response to extension, shortening and differential sedimentary loading (Vendeville and Jackson, 1992; Hudec and Jackson, 2007). *Passive* diapirism is the syn-depositional growth of salt body at/near the free surface driven by differential vertical load of sediments within surrounding minibasins; these sediments sink into the salt-source layer, thereby pumping salt into adjacent diapirs (Nelson, 1989; Jackson and Talbot, 1991; Rowan et al., 2003; Jackson and Hudec, 2017). This mechanism drives the growth of many of the world's largest diapirs, ceasing only when salt flow is outpaced by sedimentation, typically as a consequence of depletion of the salt source-layer (Rowan et al., 2003; Jackson and Hudec, 2017).

Passive diapirism is commonly linked to the subsidence of and deposition within flanking minibasins. Minibasin deformation and associated stratal thickness variations occur at two main scales: (i) minibasin-scale, which is associated with the development of broad folds that span the minibasin width; and (ii) diapir-flank-scale, which is associated with a much narrower zone of drape folding and thinning of diapir roof strata, typically within 1 km of the salt-sediment interface (e.g. Vendeville and Jackson, 1991; Rowan et al., 2003; Giles and Rowan, 2012; Rowan et al., 2014). Syn-kinematic growth strata associated with diapir-flank scale deformation are referred to as halokinetic sequences (HS), which are defined as unconformity-bounded packages of thinned and folded strata adjacent to passive diapirs (Giles and Lawton, 2002; Giles and Rowan, 2012; Hearon et al., 2014). Deformation of these strata is controlled by drape folding and upturn of ephemeral, thin diapir-roofs and associated flank strata during passive diapirism. Rotation and flexure are accommodated by layer-parallel slip, with little to insignificant vertical (i.e. diapir-parallel) shearing or drag fold (Giles and Rowan, 2012; Rowan et al., 2003; 2014; Hearon et al., 2014; Jackson and Hudec, 2017).

Giles and Rowan (2012) define two end-member styles of halokinetic sequence (HS): i) *hooks*, characterized by narrow zones of folding (<200 m), high-angle truncations (>70°) beneath bounding unconformities, and abrupt facies transitions towards the salt-sediment interface; and (ii) *wedges*, which are typified by broad zones of folding (300-1000 m), low-angle truncations (<30°) beneath bounding unconformities, and gradual facies changes towards flanking salt (Fig. 1a). These are of parasequence scale (c. 10-50 m thick), with hooks and wedges stacking to form c. 100-1000 m thick tabular and tapered composite halokinetic sequences (CHS), respectively (Fig. 1b) (Giles and Rowan, 2012). Tabular CHSs have a tabular form (parallel base and top boundaries), with axial-traces within each hook sequence being offset from each other and being oriented sub-parallel to the diapir margin (Fig. 1b). They are often associated with minor salt cusps that form where the unconformities intersect the diapir (Giles and Rowan, 2012) (Fig. 1b). Tapered CHSs have a tapered shape defined by converging upper and lower boundaries, with internal axial-traces that are inclined and curve away from the diapir margin (Fig. 1b).

These halokinetic sequence end-members are thought to be a function of the interplay between local salt-rise rate (R), local sediment accumulation rate (A) (Giles and Rowan, 2012) and, ultimately, local diapir roof thickness (Hearon et al., 2014). In cases where diapir rise-rate is greater than the sediment accumulation rate (R>A), hook HS will form, stacking to generate a tabular CHS. Conversely, wedge HS and tapered CHS sequences form when sediment accumulation rate outpaces diapir-rise rate (R<A). In the case where R>>A, the diapir will flare upward and may eventually extrude an allochthonous salt sheet, whereas if R<<A, the diapir will narrow and eventually stop rising as it is buried. These sequences were first and most thoroughly described from essentially two-dimensional, outcrop-based studies (cf. Giles and Lawton, 2002; Giles and Rowan, 2012; Saura et al., 2014; Kergaravat et al., 2016; Martín-Martín et al., 2017; Moragas et al., 2018); such studies are able to capture the high-resolution facies variations occurring within relatively thin HS, at a specific structural and/or stratigraphic position, but reveal only limited information about the four-dimensional

variability of such salt-sediment interactions. Only Hearon et al. (2014) constrain the 3D architecture and temporal variations in CHSs, in this case using seismic reflection data from the northern Gulf of Mexico. However, they only explore a single, geometrically rather simple, plug-like diapir (i.e. stock) defined by an essentially vertical salt-sediment interface.

We here use 3D time- and depth-migrated seismic data from the SE Precaspian Basin, onshore Kazakhstan to examine vertical and lateral variability in CHS architecture along diapirs (stocks and walls) with variable planform and cross-sectional geometries. We adopt a similar approach to Hearon et al. (2014), integrating seismic data and structural restorations to analyse variations of CHS architecture at the present-day as well as at the time of their formation. We also use our restorations to demonstrate, for the first time, the sequential evolution of the diapirs and associated CHS strata. We focus on answering the following questions: 1) How laterally variable are CHSs along salt walls and in thick minibasin successions?; 2) What is the relationship between CHS architecture and different diapir cross-sectional geometries (i.e. inclined, upright and salt shoulders)?; 3) What controls these architectural variations?; 4) How are diapir-flank and minibasin-scale deformation related?; and 5) What implications does CHS variability have for diapir-flank hydrocarbon-reservoir pinch-out?

2. GEOLOGICAL FRAMEWORK

The Precaspian Basin is a large (540,000km^2), elliptical basin located at the northern edge of the Caspian Sea in Kazakhstan and Russia, on the SE edge of the East European Craton, near the present southern margin of Eurasia (Fig. 2a-b). The basin initially formed in response to Devonian rifting and subsequent Carboniferous, post-rift thermal subsidence (Barde et al., 2002a,b; Volozh et al., 2003). The Ural Orogeny started in the middle Carboniferous in response to the collision of the eastern European and Kazakh plates, causing uplift of the Precaspian Basin's eastern side and the development of a rapidly-subsiding foreland basin in the remaining Precaspian Basin (Brunet et al., 1999; Barde et al., 2002b). During this time (i.e.

Kungurian-Kazanian) the basin became isolated from the Tethys Ocean and a thick (up to 4.5 km in the basin; c. 2 km in the study-area) salt sequence was deposited (Barde et al., 2002b, Volozh et al., 2003; Fernandez et al., 2017). During the Upper Permian, sedimentation was dominated by westward progradation of a non-marine clastic wedge comprising material shed off the rising Ural Mountains. This wedge loaded and expelled salt westward and up into rising diapirs (Volozh et al., 2003); and resulted in development of broadly margin-parallel, N-oriented salt walls and expulsion rollovers near the eastern basin margin (Duffy et al., 2017; Jackson et al., 2019).

Farther west and within our study-area, the salt-related structural framework is characterized by a polygonal pattern of salt walls and sub-circular minibasins (Fig. 2b), with individual walls being up to 20 km long, 8 km wide, and with up to 5.5 km of vertical relief (Duffy et al., 2017; Fernandez et al., 2017). Several Late Permian minibasins up to 1 km thick containing evaporites and non-marine clastics subsided into and are now being fully or partially encased in Lower-Middle Permian salt (Fig. 2c) (Fernandez et al., 2017). A subsequent generation of (supra-salt) minibasins formed by load-driven subsidence and passive diapirism during the Late Permian to Triassic (Duffy et al., 2017; Jackson et al., 2019). These minibasins are up to 10 km in diameter and up to 5.5 km deep, being typically welded to the pre-salt interval and/or to the encased minibasins (Duffy et al., 2017; Jackson et al., 2019). Jackson et al. (2019) show that these minibasins are characterized by lower bowl- and upper wedge-shaped units, which record periods of symmetric and asymmetric subsidence, respectively, the cause for which is unclear. Our study focusses on the geometry, stratigraphic architecture and deformation styles of diapir-flank strata within these Upper Permian-Triassic, supra-salt minibasins and their associated salt-sediment interface, which may, ultimately, help understanding the controls in the variables styles of subsidence and diapirism in the area.

The minibasins are capped by the Base Jurassic Unconformity (BJU, yellow line in fig. 2c), which records a major erosional event associated with the Late Triassic Cimmerian Orogeny. This regionally important tectonic event occurred as Gondwana-derived blocks and Tethyan

arc fragments collided with the southern margin of Eurasia, >1000 km south of the study area (Fig. 2a) (Volozh et al., 2003). Minibasins and diapirs are overlain by a gently-folded Jurassic-Lower Cretaceous section associated with several regional, Late Cretaceous-Miocene shortening events related to the collision of Arabia and India with Asia (Volozh et al., 2003; Duffy et al., 2017). The strains associated with these pulses of shortening were relatively mild in our study area due to it lying some distance from the collision front, being mostly accommodated by squeezing of diapirs between laterally mobile, relatively undeformed supra-salt minibasins (Duffy et al., 2017; Jackson et al., 2019).

3. METHODS AND DATASET

3.1. Seismic Interpretation

We use a time-migrated 3D seismic reflection dataset that covers 2532 km^2 of the eastern Precaspian Basin (Fig. 2), imaging up to 6 seconds two-way time (TWT). These data have a vertical sample rate of 2 milliseconds (ms) and inline (E-W) and crossline (N-S) spacing of 20 m. The seismic data are presented with Society of Economic Geologists (SEG) 'normal polarity', where a downward increase in acoustic impedance is represented by a positive reflection event (white on seismic sections) and a downward decrease in acoustic impedance is represented by a negative reflection event (black on seismic sections). Our time-migrated data have better imaging of supra-salt minibasin stratigraphy than the depth-migrated volume used by Duffy et al. (2017) and Fernandez et al. (2017) to analyse the more deeply buried, encased minibasins. We therefore use these time-migrated seismic data to undertake our seismic-stratigraphic analysis of the supra-salt minibasins and halokinetic sequences, using a seismic velocity volume to perform depth-conversion of key sections. Due to its better imaging of more deeply buried structures, we use the depth-migrated data to constrain the large-scale morphology of diapirs and minibasins (e.g. top-salt depth map, fig. 3), and to test the accuracy of our depth-converted sections.

Various boreholes lie within the study-area, although most are relatively shallow, terminating in Upper Triassic strata. Some wells do penetrate to deeper depths, although they targeted encased minibasins and, therefore, penetrate areas of thick-salt (i.e. diapirs) and do not intersect the intervening supra-salt minibasins (see Duffy et al., 2017; Fernandez et al., 2017). For this reason, we have limited control on the age and lithology of the supra-salt minibasin strata. However, given the Lower-Middle Permian age of the salt, and the stratigraphic position of the distinct Base Jurassic Unconformity (BJU), the minibasins are likely Late Permian-Triassic (see above). Despite the lack of borehole data, we utilize seismic-stratigraphic relationships and geometries to define and map unconformity-bounded packages (i.e. CHS) near the diapir flanks. We present CHSs preserved within three seismically well-imaged minibasins that; i.e. because of the good to excellent image quality, we can confidently map the geometry of the salt-sediment interface and the diapir-flank stratal architecture. These minibasins are also flanked by diapirs with distinct cross-sectional styles and planform geometries, allowing us to analyse the 4D variability of CHSs associated with a range of diapir types (i.e. upright vs. inclined salt walls, salt walls vs. stocks and salt shoulders).

We mapped 16-18 CHS within each minibasin in addition to mapping base- and top-salt, and the Base-Jurassic Unconformity (BJU). The definition of CHS axial-traces, and the measurements of tapering angle and width of thinning, were done by estimating an inflection point where diapir-flank related tapering and thinning begin (cf. Hearon et al., 2014). Although this can be subjective, as tested here and pointed out by Hearon et al. (2014), the variance associated with picking different inflection points is insignificant (<10%). Please note that all measurements were performed initially in the time-migrated sections and then corrected after the depth-conversions.

3.2. Depth-Conversion and Structural Restoration

The main criteria used to distinguish different types of seismically imaged CHS are the geometry and width of folding/stratal thinning (cf. Hearon et al., 2014). Given that these are

157 both broadly sub-horizontal parameters, vertical exaggeration in our time-migrated data do
158 not greatly affect any extracted values. However, to more accurately quantify the CHS
159 geometries, we perform depth-conversion for each example presented here, using the seismic
160 velocity volume mentioned above. We also perform 2D structural restorations using 2DMove©
161 to compare and quantify parameters such as tapering angles and folding zone width for both
162 present and original CHS geometries, thereby eliminating distortions caused by post-
163 depositional deformation and burial-related compaction (tables 1-3). The restoration approach
164 and quantitative analysis are based on the method defined by Hearon et al. (2014) and utilizes
165 the decompaction and flexural-slip unfolding algorithms (see Rowan et al., 2003; Rowan and
166 Ratliff, 2012 for salt restoration algorithms). Vertical decompaction was done using the Sclater
167 and Christie (1980) compaction function for sand and shale, which is appropriate given the
168 known composition of the suprasalt minibasins.

169 **4. COMPOSITE HALOKINETIC SEQUENCE VARIABILITY**

170 Suprasalt minibasins formed during the Upper Permian-Triassic in response to differential
171 loading and passive diapirism (see Jackson et al., 2019). In many of these minibasins, CHSs
172 are not visible due to: i) minibasin tilting and associated rotation of near-flank strata to near-
173 vertical due to late-stage shortening and diapir squeezing (Duffy et al., 2017) and/or ii) the
174 presence of large salt overhangs, which hampers imaging of the sub-diapir flank strata. We
175 thus focus our analysis of CHS geometry on two distinctly different diapir geometries observed
176 around three minibasins: 1) an inclined-diapir margin (Fig. 4a), and 2) a vertical salt wall that
177 passes along-strike into a salt roller (Fig. 4b). We first describe how the CHSs vary vertically
178 in individual cross-sections before assessing how they vary laterally by comparing multiple
179 cross-sections and 3D images.

180 Inclined diapir flanks (Fig 4a and left-hand side of fig. 4b) afford excellent imaging and high-
181 confidence interpretation of the salt-sediment interface and, consequently, of CHS tapering
182 and width of thinning. Where diapir flanks dip more steeply (e.g. Fig. 4b, right-hand side), the

183 precise definition of the salt-sediment interface can be, in places, problematic. In these cases,
184 the interpreted diapir flank may be slightly (20-30 m) offset from its true position (Fig. 4). The
185 distinction between different CHS end-members is therefore based primarily on the shape of
186 the sequence (i.e. degree of upturning and parallel vs. convergent bounding surfaces) and
187 secondarily on the width of folding on both present and restored sections (see section 4.2.2).

188 In all examples, the CHS are bounded by pronounced erosional unconformities that extend <
189 1 km away from the diapir margin, passing into correlative unconformities towards the
190 minibasin centre (Fig. 4). The CHS are upturned and are in direct contact with the diapir, and
191 have variable degree of folding, thinning, and structural relief (Fig. 4, tables 1-3). Where the
192 salt-sediment interface dips gently and the diapir-flank seismic imaging is best, we also
193 observe minor salt cusps where bounding unconformities intersect the diapir; these are
194 especially prominent in tabular CHS (Fig. 4a). In general, the CHS present multiple internal
195 unconformities associated with higher-order halokinetic sequences (cf. Giles and Rowan,
196 2012) and display basal onlaps at or near their axial-traces (Fig. 4). In other cases, especially
197 within tabular CHS, low-continuity-to-chaotic facies interfinger with more continuous, brighter
198 reflections near the diapir-margin, possibly indicating debris flows sourced by material eroded
199 from the diapir's crest (Fig. 4). In this study, we also define 'transitional' CHSs; these have
200 geometries and widths of folding that are intermediate (i.e. 200-300 m) between tabular and
201 tapered end-members (Fig. 4), although in most cases their shape more closely resembles
202 that of the tabular end-members (see restored sections, section 4.2).**4.1. Inclined Diapir**

203 **4.1.1. Overall geometry**

204 In our first example, we analyse the CHS architecture on the southwest flank of a semi-circular
205 minibasin associated with a c. 12 km long curvilinear salt wall that has an inclined flank (40°
206 in its lower section increasing to 60° in its upper section; figs. 5-7). The minibasin tilts to the
207 SW due to shortening-induced uplift of its NE flank; in contrast, the southwest wall and
208 associated CHS strata, which form the focus of our analysis, are largely undeformed. This

tilting made the dip of the southwest salt wall even gentler, meaning we can more confidently define the salt-sediment interface, and related CHS stratigraphic architecture, than in previous studies focused on very steep-sided salt diapirs (Fig. 4a) (cf. Hearon et al., 2014).

4.1.2. Minibasin and CHS architecture

The first stage of diapir growth was controlled by minibasin-scale subsidence as evidenced by a lower bowl-shaped stratigraphic section with a sub-vertical, synclinal axial-trace at its centre (Figs. 5-6) (cf. Rowan and Weimer, 1998; Jackson et al., 2019). The second stage was characterized by a switch in the location of depocentres towards the flank of the diapir as indicated by the large-scale wedge geometry associated with at least 16 CHS observed in profiles sub-parallel to the wedge dip-direction (Figs. 5-6). The inclined wall is flanked largely by tapered CHS (Figs. 5-6), with only two (northern section, fig. 5) and one CHS (central section, fig. 6) out of the 16 being classified as tabular (table 1).

In general, tabular CHS are relatively thinner (150-250 m at present, fig. 8 and 180-300 m decompacted, fig. 9) than tapered CHSs (150-450 m at present, fig. 8 and 180-520 m decompacted, fig. 9) and occur towards the intermediate-to-late stages of diapir rise and minibasin subsidence (i.e. in the middle and uppermost parts of the minibasin; CHSs 13-14, fig. 5 and CHS 13, fig. 6). Tabular CHS have folding and thinning zones ranging from 90-185 m of width (100-200 m restored) and taper angles of 60-64° (54-60° restored, Table 1), values that are relatively low when compared to tabular CHS associated with the upright wall (see section 4.2.). The tapered CHS have a folding and thinning zone ranging from 360-940m (420-1000 m restored) and taper angles of 8-44° (12-35° restored).

The minibasin and individual CHS become, in general, thinner southwards, with this being associated with a switch from dominantly tapered (Figs. 5-6), to a mixture of tabular and tapered CHSs (Fig. 7, table 1). CHS end-member distribution is also notably different in the south, with tabular CHS occurring in the lower and uppermost sections, and being separated by an intermediate section with tapered CHS (Fig. 7). The lower CHSs (1-6), which have

typical tapered geometries in the northern and centrals sections (Figs. 5-6), have, in the south, a narrow (< 100 m) zone of folding and thinning towards the diapir, with prominent salt cusps intercepting their unconformities (Fig. 7, table 1) (cf. Giles and Rowan, 2012; Hearon et al. 2014). These CHS also become condensed to the south, being only c. 80-100 m thick (fig. 7), which is equivalent to the thicknesses of higher-order, halokinetic sequences (Giles and Rowan, 2012). CHS 14-16, despite maintaining their thickness, also switch southwards from tapered to tabular (Fig. 5-7, table 1).

The lowermost CHSs (1-4, table 1) present more unique lateral variations, demonstrating the increasing influence of larger, minibasin-scale folding and subsidence towards the centre of the salt wall (Figs. 5-6). Although, their geometries are indicative of diapir-flank processes, i.e. their thinning and folding still occurs near the diapir margin, the width of the folding zone increases up to 2100 m away from the diapir and taper angles are considerably lower (11-14° restored, table 1, fig. 8).

4.1.3. Diapir and Minibasin Evolution

The dominance of tapered CHSs in the inclined diapir example suggests that the development of gently-inclined salt walls is associated with a predominantly higher sediment accumulation rate (A) relative to the net salt-rise rate (R) (and/or volumetric salt flux (q); cf. Jackson and Hudec, 2017) (Figs. 5-6 and 8-9). This interpretation is supported by the fact that the wall exhibits a subtle steepening of its margin through time (from c. 40 to 60°) that correlates with a general upward narrowing of the zone of folding and thinning of minibasin strata (Table 1 and fig. 9), which, in turn, implies a relative increase of R/A or q/A.

The CHS geometries and distribution are also variable along-strike as shown by the greater proportion of tabular CHS geometries to the south (Fig. 7), where the salt wall is also steeper (Figs. 5-7). This southward transition from tapered to tabular CHS geometries may be associated with: i) significant thinning of individual CHS (e.g. CHS 1-5) and, thus, a lateral decrease in the sediment accumulation rate that resulted in increase in R/A or q/A; or ii) along-

strike variations in diapir-rise rate (R or q) in the cases where CHS thickness does not vary along-strike (e.g. CHS 14-16). The latter may thus be better explained by volumetric (i.e. 3D) salt flux variations and local variations of roof thickness and width, rather than the classical two-dimensional A/R ratios (cf. Giles and Rowan, 2012) (see discussion).

4.2. Vertical salt wall

4.2.1. Overall Geometry

Our second example comes from two adjacent minibasins flanking a 3-4 km tall, 3 km long and 1-2 km wide, N-trending salt wall (Fig. 3). The diapir is upright and has a sub-vertical upper flank and a more gently-dipping lower flank (Fig. 10). It varies in shape and dimension along-strike, passing northwards into a smaller diapir containing a 1.5 km wide salt shoulder (*sensu* Giles et al. 2018) half-way up its western flank (Fig. 11), and ultimately into a salt roller (sensu Vendeville and Jackson, 1992a) at its northern end (Fig. 12). Because the two minibasins are connected around the diapir and roller at their northern end, it is possible to constrain the relative ages of CHSs on both sides of the diapir (Figs. 4-6.). This provides a unique opportunity to analyse how: i) a single CHS can vary across a salt wall with laterally variable cross-sectional geometry, ii) how two minibasins associated with the same salt wall can have variable CHS architecture, and iii) how CHSs transition from halokinetically-driven diapirs (passive and/or active) to diapirs driven by extension (i.e. reactive).

4.2.2. Minibasin and CHS architecture

The diapir is flanked on both sides by CHS (Figs. 10-11). Both minibasins contain a lower, 1-1.5 km thick, bowl-shaped section, which is c. 400 m thicker in the western minibasin than in the eastern minibasin (Fig. 10). This section thins northwards, towards the edge of the salt diapir, with age-equivalent strata showing typical CHS geometries (i.e. narrow zones of folding and thinning). The overlying stratigraphic succession is composed of strata that are of broadly constant thickness (on average 90-320 m thick at present-day) towards the minibasin centre,

but which display localized (< 1 km) thinning and folding near the salt-sediment interface, characteristic of CHSs (tapered and tabular) (Figs. 10-11).

There are drastic variations in the geometry and distribution of CHSs between the two partially-connected minibasins (Figs. 10-11). In Section 1, the western minibasin is dominated by tapered CHSs from the earliest-to-intermediate (CHSs 1-12) to final stages of diapir growth (CHSs 17-18), with only four non-tabular (e.g. tapered and transitional) CHSs in the intermediate-upper section (CHSs 13-16, fig. 10, table 2). The tapered CHSs are characterized by thinning and folding zones ranging from 370-1970 m (350-1180 m restored) with an average of 830 m (720 m restored), and taper angles of 13-49° (11-30° restored), with an average of 31° (18° restored) (Table 2). The tabular CHSs have folding zones ranging from 45-190 m (30-155 m restored) with an average of 100 m (present-day and restored) and taper angles of 52-74° (50-72° restored), with an average of 64° (60° restored) (Table 2). Conversely, the eastern minibasin is dominated by tabular rather than tapered CHSs, with only two tapered (CHS 2 and 10) and two transitional CHSs (CHS 1 and 5). The two tapered CHS have thinning and folding zones ranging from 300-810 m (310-915 m restored) and taper angles of 18-26° (17-18° restored) (Table 2). The tabular CHS have folding zones varying from 45-190 m (45-170 m restored) with an average of 96 m (109 m restored), and with taper angles of 40-71° (36-68° restored), with an average of 57° (52° restored) (table 2).

Only CHSs 2, 10 and 14-16 have the same end-member geometries across the diapir; they do however differ in terms of their width and taper angle (Table 2). They also differ in terms of their thickness, with CHSs being generally thicker on the western, tapered CHS-dominated minibasin (Figs. 10 and 13a). The largest thicknesses contrasts occur within CHSs 3-7, which are tapered and up to 320 m thick on the west minibasin, and tabular and only 90-150 m thick in the east minibasin (Fig. 13a). This CHS variability can be linked to changes in the diapir flank morphology (Fig. 4). The lower-to-intermediate diapir section (between CHSs 1-5) has a more gently-dipping (c. 40-50°) flank, with a series of narrow (c. 300-500 m), sub-horizontal (15-30°) salt shoulders on the west where tapered CHSs predominate (Fig. 10). Conversely,

313 the equivalent, lower-to-intermediate eastern diapir flank is steeper (55-65°), has no
314 recognizable salt shoulder and is largely associated with tabular CHSs (Fig. 10). The upper
315 diapir flanks are sub-vertical (c. 90°) on both sides and predominantly associated with tabular
316 CHSs (CHSs 13-16) in both minibasins, although the final two (CHS 17-18) are characterised
317 by tapered and tabular geometries on the west and east minibasin section, respectively (Fig.
318 4).

319 Section 2, another dip-oriented section located 1.2 km further north of Section A, demonstrates
320 how CHS and diapir geometries vary significantly over a relatively short along-strike distance
321 (Fig. 11, table 3). In this location the salt wall is shorter (c. 2.8 km tall) and is defined by a
322 broader (1.5 km wide), clearly-defined salt shoulder relative to Section A (Fig. 10). Strata age-
323 equivalent to CHSs 13-18 from Section A (Fig. 10) are not classified as CHS because they
324 cover the diapir and show no diapir-related thickness variations (Fig. 11). The tabular CHSs,
325 all in the western minibasin, have present folding zones varying from 20-200 m (average of
326 93 m) and taper angles from 42-86° (average of 65°) (Fig. 11, table 3). The tapered CHSs
327 have a 325-1100 m wide zone of folding (average of 480 m) and are defined by tapers angles
328 of 11-49° (average of 30°) (Fig. 11, table 3).

329 The eastern minibasin in Section 2 shows a similar distribution of CHSs to that seen in Section
330 A (Fig. 10), but with a significantly greater proportion of tabular geometries (i.e. all but the last
331 CHS are tabular; Fig. 11, table 3). The western minibasin, however, exhibits more marked
332 along-strike variations; it has no tabular CHSs and contains CHSs (2-5) that are downturned
333 and thickened towards the diapir (Fig. 11). The restored geometries indicate 10-15% of
334 localized stratal thickening into the axes of near-diapir synclines or rollovers above the salt
335 shoulders (Fig. 13b). All other CHSs (1 and 6-12) are tapered. CHSs 2-5 thus differ to
336 previously described CHSs given they are rotated downward and thicken into a near-diapir
337 rollover; ultimate thinning towards the diapir simply reflects stratigraphic onlap onto the
338 inclined salt-sediment interface, rather near-diapir upturn (see Fig. 1, Giles and Rowan, 2012).
339 They are, nonetheless associated with classic tapered CHS geometries and diapir flank-

related deformation 1 km further south, i.e. thickness variations and folding occur within 370-680 m from the salt-sediment interface. The kinematics of this different style of CHS with the synclinal-rollover geometry over an area of pronounced narrowing of the diapir (i.e. salt shoulder) will be addressed in Section 5.2.

1.2 km further northward (Section 3), the salt-related structural style changes from a diapir to that of a normal fault-bound salt roller nucleating onto gently inflated salt (Figs.10-12). The upper salt roller is defined by an east-dipping listric normal fault that is overlain by a west-verging extensional rollover. The age-equivalent stratal architecture seen here is notably different from that seen further south. More specifically, minibasins strata do not display typical CHS geometries (i.e. diapir flank upturning and thinning). Instead, sequences 1-10 are all downturned towards the roller on both of its sides, with sequences on the eastern side also thickening towards the roller-bounding fault (Fig. 12). Strata are broadly isopachous on the footwall, although subtle thinning occurs between sequences 1-3, which onlap the earlier diapir. Sequences 1-3 may thus be classified as tapered CHS that were later collapsed and downturned due to extension (Fig. 12).

The unique along-strike variations in CHS architecture and diapir morphology described above are best visualized in 3D (Fig. 14). This 3D image shows how a single CHS transitions from: i) a tabular geometry with abrupt thinning towards the diapir eastern flank to, ii) localized downturn above a salt shoulder to the northwest, and to, iii) a tapered geometry that extends 350 m upward along the western diapir flank (Fig. 14). Northwards, towards the axis of the larger depocentre, the CHS gives way to fault-related hangingwall thickening towards a roller-bounding normal fault, until it switches again to typical CHS geometries associated with a different salt wall further north (Fig. 14).

4.2.3. Diapir and Minibasin Evolution

Sequential structural restorations illustrate the evolution of the salt wall and associated growth strata, helping explain the observed CHS variability along the two, partially-connected

minibasins (Figs. 15 and 16, supplementary material). The restoration demonstrates that the diapir grew passively and asymmetrically since its earlier stages, with a gentler western flank and steeper eastern flank (Figs. 15-16). This style of growth is recorded in the CHS architecture; i.e. the development of tapered CHSs on the gently-dipping, western flank and tabular CHS on the more steeply-dipping, eastern flank. Moreover, the restorations also show that the coeval development of different CHS end-members on each side of the diapir is associated with how far syn-kinematic strata extends across the diapir flank and/or onto its crest (Fig. 15). The CHS therefore formed as temporary roofs that were shouldered aside and upturned due to continuous salt rise (cf. Rowan et al., 2003) (Figs. 15-16).

The restorations also show how the development of tapered geometries that extend 200-350 m along the western flank of the diapir (CHSs 1-9) is related to the occurrence of salt shoulders. These narrow shoulders are partially destroyed due to continuous salt rise, which also reduces the diapir asymmetry and overall width, and further rotates previously-deposited CHSs (Fig. 15). Some of these early tapered CHSs formed small-scale anticline-syncline pairs along the flank of the diapir as they onlapped supra-shoulder strata and/or the shoulder itself (CHSs 2-4, fig. 15, supplementary material). These units may record brief episodes of relatively minor shoulder-collapse due to dissolution and/or salt expulsion (cf. Giles et al., 2018). The width of the salt shoulders varied along-strike (Figs. 15 and 16). Where it formed a km-scale feature, supra-shoulder strata collapsed and downturned above it, forming a rollover with localized thickening towards the diapir (CHSs 2-5, fig. 16).

5. DISCUSSION

5.1. How laterally and vertically variable are Composite Halokinetic Sequences?

Our study confirms the hypothesis of Hearon et al. (2014) that different CHS end-members can form along the same diapir at the same time. However, we demonstrate that CHSs can vary even more drastically and frequently across salt diapirs than previously described. All CHSs analysed here have laterally variable drape-fold widths, taper angles and relief (Figs. 5-

7, 10-11 and Tables 1-3). This corresponds to an overall greater lateral variability than observed by Hearon et al. (2014), where only three CHSs (<10% of the total number analysed) varied along-strike. These variations can be relatively subtle so that the CHS end-member does not change. In many cases, however, CHSs can vary from one end-member to another within the same minibasin and over only <1 km along strike (Figs. 5-7 and 10-11, tables 1-3). A single CHS can also vary between tabular and tapered end-member geometries along-strike and across the same diapir, and within two different, albeit partially-connected minibasins (Figs. 10-11, tables 2-3). CHS relief can also change significantly (c. 100-300 m) along an individual CHS, especially in the case of tapered end-members that can have up to 400 m of structural relief (cf. CHSs 5 and 7-11, figs. 6; CHSs 4, 6 and 8, fig. 10).

These sequences can also transition *laterally*, over very short length-scales (c. 1 km), from classical CHS (i.e. locally upturned and thinned) into rollover CHSs with localized stratal thickening above salt shoulders, fig. 11). They can also switch laterally into normal-fault-driven thickened strata overlying salt rollers, or even into isopachous and relative undeformed strata away from the diapir and, thus, not being classified as CHSs (Figs. 11-12). These sequences can also transition along-strike from being controlled by diapir-flank scale deformation, to being influenced and even driven by minibasin-scale subsidence towards their centre (cf. Rowan et al., 2016). Such transitions are more common within deeper, older CHSs (Figs. 5-6 and table 1, see section 5.4).

The classic CHS succession consists of lower tapered, intermediate tabular, and upper tapered CHSs (Giles and Rowan, 2012; Hearon et al., 2014). The stratigraphic transition from lower tapered CHSs to tabular CHSs is associated with an increase in the rate of salt-rise as the minibasin gradually thickens, becomes denser, and pumps salt more rapidly into the flanking diapirs. As a continuum of this process, the source-layer is gradually depleted, resulting in a decrease in the salt-rise rate and, as a consequence, a switch from tabular to tapered CHSs (Giles and Rowan, 2012). Our work shows that switches from tabular to tapered end-members can be more frequent than previously documented (Table 2). These switches

are commonly linked to marked changes in diapir shape, such as those occurring in association with salt shoulders (Figs. 10-11 and 15-16) (see section 5.2). Moreover, the CHS succession can also display vertical patterns that differ to the classical three-part vertical zonation (Figs. 7 and 10-11, tables 1-3). For example, the vertical wall is flanked on the east by a minibasin dominated by tabular CHS (Fig. 10, table 3). In contrast, the minibasin to the west is defined by the classic tapered-tabular-tapered vertical zonation (Fig. 10, table 3). The inclined wall displays a more typical zonation along most of its length, having a dominantly tapered CHS succession, with only a few tabular CHSs towards its top. However, towards the south, this zonation is different, with the lower and uppermost sections being composed of tabular CHSs with intermediate tapered CHSs (Fig. 7, table 1).

5.2. What is the interplay between different diapir cross-sectional geometries and CHS architecture?

5.2.1. Geometrical variations between different diapirs

This study provides the first-ever analysis of CHS architecture adjacent to diapirs with differing flank geometries. Diapirs with sub-vertical margins are flanked a greater proportion of tabular CHSs (27% on west minibasin to 78% on east minibasin) relative to inclined diapirs (8-50%). This suggests that, for diapirs with sub-vertical flanks and at a CHS time-scale, diapir-rise rate is generally greater than sediment accumulation rate when compared to inclined diapirs. This example also shows that even broadly symmetric diapirs can be flanked by minibasins with highly-asymmetric stratigraphic architectures. Age-equivalent strata on both sides of the diapir display, in most cases, contrasting end-member CHS geometries and up to 80-100% of thickness variations (Figs. 10-11, 13 and tables 2-3). Such asymmetric subsidence (Figs. 15-16) can be related to three-dimensionally complex patterns of salt flow and diapir rise (Jackson et al., 2019; Fernandez et al. 2019).

The example of a diapiric wall with an inclined margin shows that, in addition to a generally greater proportion of tapered CHSs, the ratio of tapered CHS (to tabular or transitional CHSs)

445 is higher towards their centre (Figs. 5-7 and table 1). The width of the folding/thinning zone
446 commonly increases, and taper angles of tapered CHSs typically decreases, towards the
447 centre of the wall (CHSs 7-16, table 1; although see CHSs 17-19 in table 1 for an exception).
448 Ultimately, this demonstrates laterally variable diapir-rise rate and minibasin subsidence
449 through time (cf. Jackson et al., 2019; Fernandez et al., 2019). The gently-dipping diapir
450 margin and the related architecture of the flank strata suggest that in the case of inclined walls,
451 sediment accumulation-rate tends to be greater than diapir-rise rate, which is the opposite to
452 that inferred for vertical walls. As salt diapirs typically grow vertically when salt-flow rates equal
453 sediment aggradation rates (Vendeville and Jackson, 1991; McGuiness and Hossack, 1993),
454 sedimentation accumulation rate is expected to be slightly higher than salt-rise rate at CHS
455 time-scales for inclined diapirs. Nonetheless, at a longer, minibasin-time-scale, salt rise can
456 still keep pace with sedimentation as evidenced by continuous salt rise. The initial rise of
457 inclined walls is dominated by minibasin-scale subsidence and deformation as indicated by
458 the presence of an up to 2.5 km thick bowl-shaped lower sequence (Fig. 6); this contrasts with
459 the vertical walls, for which we infer a shorter period of minibasin-scale subsidence based on
460 the presence of a significantly thinner (c. 200-500 m) bowl-shaped lower interval (Figs. 10-
461 11).

462 **5.2.2. Salt Shoulders**

463 Salt shoulders are zones of abrupt diapir narrowing due to differential salt-rise from the diapir
464 margin to its centre as a function of salt supply, dissolution and roof thickness (Giles et al.,
465 2018). We recognise salt shoulders in our study-area, with the related stratal architecture and
466 transition patterns between non-shoulder and shoulder-related strata being characterized by:
467 i) a switch from tabular CHS to tapered CHS, ii) a marked increase in the width of folding and
468 thinning of tapered CHSs, and iii) rollovers within which strata dip in towards and thicken into
469 the hinges of near-diapir flank synclines. The simpler scenario (i) is the abrupt change between
470 tabular and tapered CHS end-members occurs over a narrowing salt-sediment interface (Fig.
471 17, CHS 3-4). In this case, there is a drastic increase in the width of folding, from c. 100 m

below to 650 m above the shoulder and over the erosional unconformity defining the top of a series of tabular CHSs (Fig. 17). In the second case (ii), similar increases in the width of the folding and thinning zone occur without changes to a different CHS end-member. This is seen along the western flank of the vertical wall by a pronounced lengthening (in the order of 170-300 m) of the zone of folding between tapered CHSs 4 and 5, 5 and 6, and 6 and 7 (Figs. 10 and 15, table 2).

The third shoulder scenario (iii) presents a more complex and remarkable supra-shoulder stratal architecture. In this case, pre-shoulder CHSs transition upwards over the shoulder into downturned and folded sequences that thicken towards the diapir (CHSs 2-5, Fig. 11). Their characteristic rollover and synclinal thickening geometries may suggest: i) salt expulsion from the shoulder towards the central part of the diapir, ii) an extension-driven faulted-contact, or iii) shoulder collapse due to dissolution (Giles et al., 2018). Although the third option seems more likely, our current knowledge and limited published data on salt shoulders (cf. Giles et al., 2018) do now afford a distinction between these three processes.

5.3. What controls CHS variations?

Different CHS end-members are likely a function of the relative rates of salt-rise (R) and sediment accumulation (A) (Giles and Rowan, 2012) or, more precisely, local diapir-roof thickness (Hearon et al., 2014). We concur with these hypotheses, but we add that diapir rise and sediment accumulation rates (and thus roof thickness) can vary *along* and *across* diapirs. We argue below that this variability may be ultimately driven by three-dimensional variations in the rate of diapir-rise (i.e. volumetric salt flux), something not depicted in previous CHS models (Fig. 18).

Variable sediment accumulation and volumetric salt flux generate thickness variations within individual CHSs (Figs. 5-8, 10-13). These variations may be a function of the direction of sediment input into the minibasin, and differential erosion and/or subsidence around the diapir flank and on its crest. Indeed, local sediment input direction and accumulation may have

498 influenced roof thickness in the case of the two partially-connected minibasins separated by a
499 vertical salt wall, as suggested by pronounced changes (by up to 100%) in CHSs thickness
500 around the wall (see restored CHSs 4 and 7, fig. 13). Consequently, the CHS end-member
501 type varies for age-equivalent strata across the diapir with thicker tapered geometries on one
502 side and thinner tabular geometries on the other (Figs. 10-11 and tables 2-3). This is expected
503 given that tapered CHSs are typically associated with relatively higher sediment accumulation
504 rates than tabular CHSs (Giles and Rowan, 2012). Overall minibasin thickness and
505 subsidence are logically also greater where CHS are dominantly tapered and thicker, i.e. the
506 western minibasin in Figs. 10 and 11.

507 However, this is not consistently observed within all age-equivalent CHSs, nor for the inclined
508 wall case as CHS architecture also varies regardless of overall thickness (e.g. CHSs 8-9 and
509 11, with equal thickness and different end-member geometries, fig. 13). This suggests that
510 something else, in addition to sediment accumulation rate, controls CHS style. We argue that
511 the near-diapir thickness variations characteristic of CHSs are controlled by how far the related
512 strata extended inboard above the flanking diapirs, and that this is potentially governed by the
513 three-dimensionally variable salt flux (q) within the diapir. This is seen in our restorations
514 where CHSs of broadly equal thickness across the diapir are characterized by distinct taper
515 angles and drape-fold widths, principally because of how far they originally extended across
516 the diapir crest (CHSs, 8-9 and 11, Figs. 15, 18 and supplementary material). Consequently,
517 tapered CHSs are commonly associated with gentler and wider diapir margins than tabular
518 CHSs. Progressive diapir rise, nonetheless, displaces and rotates the CHS salt-sediment
519 interfaces from an initially crestal position to the sides of the diapir, partially masking their
520 original shape and extent (Figs. 9, 15 and 16). In addition, erosion may also remove parts of
521 or, in fact, the entire diapir roof so that CHS may have extended further across the diapir crest
522 than is currently inferred from the size and geometry of the preserved wedges.

523 Restorations also demonstrate that tapered CHS can occur over transient salt shoulders that
524 record a period of diapir narrowing. We note that this may occur on only one flank of the diapir

(Fig. 15). Tapered CHS that extend for >200 m along the present-day flank of the diapir (Figs. 6, 9, 10 and 11) were originally formed over transient salt shoulders. These salt shoulders may be preserved depending on the degree of subsequent diapirism and differential diapir-rise. We thus suggest that, in addition to i) diapir-flank dissolution-collapse, ii) greater roof erosion at the diapir centre and iii) fault-related weakening of the central roof (cf. Giles et al., 2018), salt shoulders can also develop due to: iv) roof thickness variations associated with tapered CHSs that extend further inboard over the diapir.

5.4. How CHSs interact with minibasin-scale subsidence?

At early stages of diapir rise and minibasin formation, subsidence is dominantly accommodated by broad, multi-km-scale synclinal folding, and stratal thinning and onlap towards the diapir (i.e. bowl-shaped minibasins, Figs. 5-6 and 10). In later stages, subsidence tends to be more evenly distributed across the minibasin, with deformation focused near the diapir margin, resulting in the development of stacked halokinetic sequences (Giles and Rowan, 2012; Hearon et al., 2014). Our restorations show that, although primarily controlled by diapir-flank processes, CHS typically display subtle thickness variations (c. 5-15% of their maximum thickness) over a much larger (> 1 km of width) scale (Figs. 8 and 13).

The influence of minibasin-scale processes on CHS geometry is variable in time and space. It is typically greater within lower sequences (CHS 1-3 in fig. 5-6; CHSs 1-4 in fig. 10), immediately after the bowl-shaped sequence, which indicates a transitional period in which subsidence and deformation are roughly equally influenced by diapir-margin and minibasin processes. As a consequence, the definition of CHS axial-trace for the lowermost sequences can be complicated by the greater influence of larger wavelength, and minibasin-scale folding and thinning. Minibasin-scale subsidence is also more important towards the central portions of linear salt walls where lowermost sequences are controlled by minibasin-scale processes, passing laterally towards their edges into CHSs (CHSs 1-2, figs. 5 and 6, table 3). Ultimately,

this demonstrates that diapir-flank and minibasin-scale deformation work in tandem and, in most cases, as a continuum process.

5.5. Implications for hydrocarbon reservoirs

The recognition of km-scale, four-dimensional variability of HS and CHS has implications for the understanding of potential hydrocarbon reservoir distribution within minibasins and the development of diapir-flank stratigraphic (i.e. pinch-out) traps. Reservoir sandstones deposited in channels and lobes will tend to accumulate downdip of diapir-related topographic relief (Matthews et al., 2007; Banham and Mountney, 2013; Hearon et al., 2014). This means that reservoirs will pinch-out updip, at or near the axial traces of drape folds developed within CHSs (Fig. 4) (Giles and Rowan, 2012; Hearon et al., 2014). Tabular CHS may, therefore, have reservoir facies that are in direct contact with the diapir or that pinch-out less than 200 m away from it. In contrast, tapered CHS may contain reservoirs that pinch-out 300-1000 m away from the diapir (Fig. 4). As CHSs vary along-strike and across salt walls, reservoir distribution and pinch-out will also vary. The same CHS may have reservoir facies in direct contact with the salt wall on one side and > 300 m away from the diapir on its other side (Fig. 18). Although our work focuses on fluvial-continental and clastic-dominated minibasins, the observed geometric variability of diapir-flank strata can also be applied to shallow- and deep-waters settings influenced by diapirism and, ultimately aid the prediction of reservoir-facies and pinch-out location within minibasins.

6. CONCLUSIONS

This study combines 3D seismic and 2D structural restorations to analyse the interaction between diapirism with minibasin subsidence and deformation, focusing on diapir-flank architecture and development of composite halokinetic sequences. We provide for the first time, a 3D, seismic-based study that evaluates the development of composite halokinetic sequences associated with different geometries and styles of diapirs, demonstrating that CHSs can be highly variable through time and space. We analyse CHS variability within a

single minibasins along an inclined salt wall; and within two different minibasins across an upright, broadly vertical salt wall. A single CHS can vary along-strike within the same minibasin and across a diapir. Their large majority (c. 73%) varies laterally across a salt wall, presenting contrasting end-member (i.e. tabular or tapered) geometries. They can also transition into isopachous and broadly undeformed strata away from the diapir or to growth strata associated with salt-related extension or diapir-collapse (i.e. rollovers). These lateral variations can be linked to changes in CHS thickness and/or in the diapir flank geometries. Tabular CHSs are commonly associated with steeper diapir flanks and tapered CHSs with relatively gentler salt-sediment interfaces. CHSs can also be more vertically variable than previously described, presenting more frequent switches in their geometries through the stratigraphic succession or different vertical zonations to the classic CHS models. These are often associated with changes in diapir geometry such as salt shoulders, which are characterized by an abrupt narrowing and gentling of the salt-sediment interface. These features are typically associated with a marked increase in the width of folding between pre- and post-shoulder CHSs, which can result in the development of different end-member geometries. They can also produce localized downturn and rollover geometries driven by diapir collapse by dissolution.

We explain that these variations are controlled by the three-dimensionally variable length and width of the diapir's roof, which is in turn controlled by a volumetrically variable salt flux and sediment accumulation, as opposed to the two-dimensional A/R ratios from previous works. Ultimately, this study improves the understanding of 3D geometries and variability of diapir-flank strata and associated salt-sediment interface. This may, in turn, aid in the prediction of sedimentary facies and trap geometries within minibasins and contribute to hydrocarbon exploration in diapiric provinces worldwide.

ACKNOWLEDGMENTS

Special thanks to Oliver Duffy and Mark Rowan for discussions. We also thank Kate Giles, Bruce Trudgill and Juan Martín-Martín for their very constructive reviews and positive criticism,

602 and Craig Magee for the editorial handling. We thank Condor Petroleum for permission to use
603 and publish the seismic data in this study. We also thank Schlumberger for the academic
604 licenses of seismic interpretation software, Petrel©, and Petroleum Experts for 2D Move©,
605 which was used for depth-conversion and structural restorations.

606 **REFERENCES**

607 Banham, S. G., & Mountney, N. P. (2013). Evolution of fluvial systems in salt-walled mini-
608 basins: a review and new insights. *Sedimentary Geology*, *296*, 142-166.

609 Barde, J. P., Chamberlain, P., Galavazi, M., Harwijanto, J., Marsky, J., Gralla, P., & van den
610 Belt, F. (2002a). Sedimentation during halokinesis: Permo-Triassic reservoirs of the Saigak
611 field, Precaspian basin, Kazakhstan. *Petroleum Geoscience*, *8*(2), 177-187.

612 Barde, J. P., Gralla, P., Harwijanto, J., & Marsky, J. (2002b). Exploration at the eastern edge
613 of the Precaspian basin: Impact of data integration on Upper Permian and Triassic
614 prospectivity. *AAPG bulletin*, *86*(3), 399-415.

615 Brunet, M. F., Volozh, Y. A., Antipov, M. P., & Lobkovsky, L. I. (1999). The geodynamic
616 evolution of the Precaspian Basin (Kazakhstan) along a north–south
617 section. *Tectonophysics*, *313*(1-2), 85-106.

618 Duffy, O. B., Fernandez, N., Hudec, M. R., Jackson, M. P., Burg, G., Dooley, T. P., & Jackson,
619 C. A. L. (2017). Lateral mobility of minibasins during shortening: insights from the SE
620 Precaspian Basin, Kazakhstan. *Journal of Structural Geology*, *97*, 257-276.

621 Fernandez, N., Duffy, O. B., Hudec, M. R., Jackson, M. P., Burg, G., Jackson, C. A. L., &
622 Dooley, T. P. (2017). The origin of salt-encased sediment packages: observations from the
623 SE Precaspian Basin (Kazakhstan). *Journal of Structural Geology*, *97*, 237-256.

624 Fernandez, N., Hudec, M. R., Jackson, C. A. L., Dooley, T. P., & Duffy, O. B. (2019). The
625 competition for salt and kinematic interactions between minibasins during density-driven
626 subsidence: observations from numerical models. https://doi.org/10.31223/osf.io/jak5u

627 Giles, K. A., Lawton, T. F. (2002). Halokinetic sequence stratigraphy adjacent to the El
628 Papalote diapir, northeastern Mexico. *AAPG bulletin*, *86*(5), 823-840.

629 Giles, K. A., & Rowan, M. G. (2012). Concepts in halokinetic-sequence deformation and
630 stratigraphy. *Geological Society, London, Special Publications*, *363*(1), 7-31.

631 Giles, K. A., Rowan, M.G., Langford, R., McFarland, J., Hearon, T. (2018) Salt Shoulders *in*
632 *AAPG Search and Discovery, AAPG International Conference and Exhibition, London,*
633 *England.*

634 Hearon, T. E., Rowan, M. G., Giles, K. A., & Hart, W. H. (2014). Halokinetic deformation
635 adjacent to the deepwater Auger diapir, Garden Banks 470, northern Gulf of Mexico: Testing
636 the applicability of an outcrop-based model using subsurface data. *Interpretation*, *2*(4), SM57-
637 SM76.

638 Hudec, M. R., & Jackson, M. P. (2007). Terra infirma: Understanding salt tectonics. *Earth-*
639 *Science Reviews*, *82*(1-2), 1-28.

640 Jackson, M. P. A., & Talbot, C. J. (1991). *A glossary of salt tectonics*. Bureau of Economic
641 Geology, University of Texas at Austin.

642 Jackson, M. P., & Hudec, M. R. (2017). *Salt tectonics: Principles and practice*. Cambridge
643 University Press.

644 Jackson, C. A. L., Duffy, O. B., Fernandez, N., Dooley, T. P., Hudec, M. R., Jackson, M. P., &
645 Burg, G. (2019). The Stratigraphic Record of Minibasin Subsidence, Precaspian Basin,
646 Kazakhstan. *Basin Research*.

Kergaravat, C., Ribes, C., Legeay, E., Callot, J. P., Kavak, K. S., & Ringenbach, J. C. (2016). Minibasins and salt canopy in foreland fold-and-thrust belts: The central Sivas Basin, Turkey. *Tectonics*, *35*(6), 1342-1366.

Martín-Martín, J. D., Vergés, J., Saura, E., Moragas, M., Messager, G., Baqués, V., Razin, P., Grélaud, C., Malaval, M., Joussiame, R., Casciello, E., Cruz-Orosa, I., Hunt, D. W. (2017). Diapiric growth within an Early Jurassic rift basin: the Tazoult salt wall (central High Atlas, Morocco). *Tectonics*, *36*(1), 2-32.

Matthews, W. J., Hampson, G. J., Trudgill, B. D., & Underhill, J. R. (2007). Controls on fluviolacustrine reservoir distribution and architecture in passive salt-diapir provinces: Insights from outcrop analogs. *AAPG bulletin*, *91*(10), 1367-1403.

Moragas, M., Vergés, J., Saura, E., Martín-Martín, J. D., Messager, G., Merino-Tomé, Ó., ... & Joussiaume, R. (2018). Jurassic rifting to post-rift subsidence analysis in the Central High Atlas and its relation to salt diapirism. Basin Research, 30, 336-362.

Nelson, T. H. (1989). Style of salt diapirs as a function of the stage of evolution and the nature of the encasing sediments. In *Gulf Coast Section SEPM Foundation 10th Annual Research Conference Program and Abstracts* (pp. 109-110).

Rowan, M. G., & Weimer, P. (1998). Salt-sediment interaction, northern Green Canyon and Ewing bank (offshore Louisiana), northern Gulf of Mexico. *AAPG bulletin*, *82*(5), 1055-1082.

Rowan, M. G., Lawton, T. F., Giles, K. A., & Ratliff, R. A. (2003). Near-salt deformation in La Popa basin, Mexico, and the northern Gulf of Mexico: A general model for passive diapirism. *AAPG bulletin*, *87*(5), 733-756.

Rowan, M. G., Giles, K. A., Hearon IV, T. E., & Fiduk, J. C. (2016). Megaflaps adjacent to salt diapirs. *AAPG Bulletin*, *100*(11), 1723-1747.

670 Rowan, M. G., & Ratliff, R. A. (2012). Cross-section restoration of salt-related deformation:
671 Best practices and potential pitfalls. *Journal of Structural Geology*, *41*, 24-37.

672 Saura, E., Vergés, J., Martín-Martín, J. D., Messager, G., Moragas, M., Razin, P., ... & Hunt,
673 D. W. (2014). Syn-to post-rift diapirism and minibasins of the Central High Atlas (Morocco):
674 the changing face of a mountain belt. *Journal of the Geological Society*, *171*(1), 97-105.

675 Sclater, J. G., & Christie, P. A. (1980). Continental stretching: An explanation of the post-Mid-
676 Cretaceous subsidence of the central North Sea Basin. *Journal of Geophysical Research:*
677 *Solid Earth*, *85*(B7), 3711-3739.

678 Volozh, Y. A., Antipov, M. P., Brunet, M. F., Garagash, I. A., Lobkovskii, L. I., & Cadet, J. P.
679 (2003). Pre-Mesozoic geodynamics of the Precaspian basin (Kazakhstan). *Sedimentary*
680 *Geology*, *156*(1-4), 35-58.

681 Vendeville, B. C., & Jackson, M. P. (1992). The rise of diapirs during thin-skinned
682 extension. *Marine and Petroleum Geology*, *9*(4), 331-354.

683 ***FIGURES***

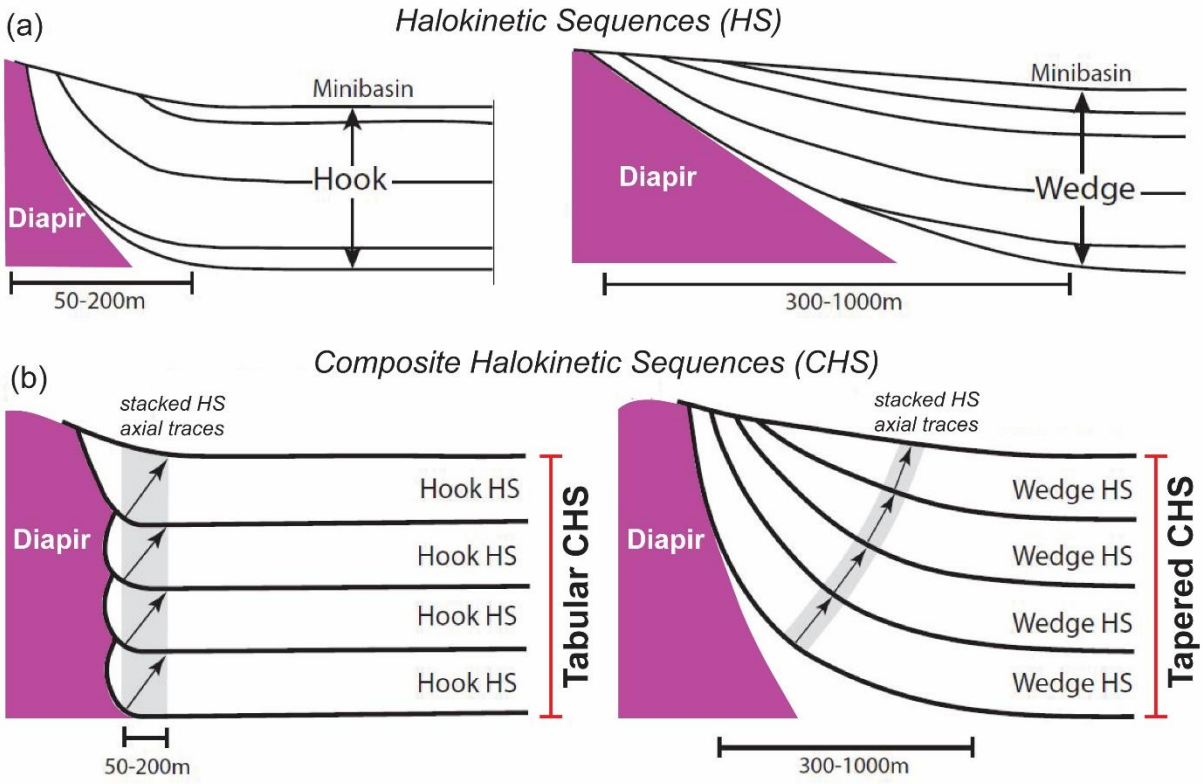

684

685 *Figure 1: (a) End-members of halokinetic sequences (HS), hooks and wedges. (b) End-members of*

686 *composite halokinetic sequences (CHS), tabular and tapered. Adapted from Giles and Rowan (2012).*

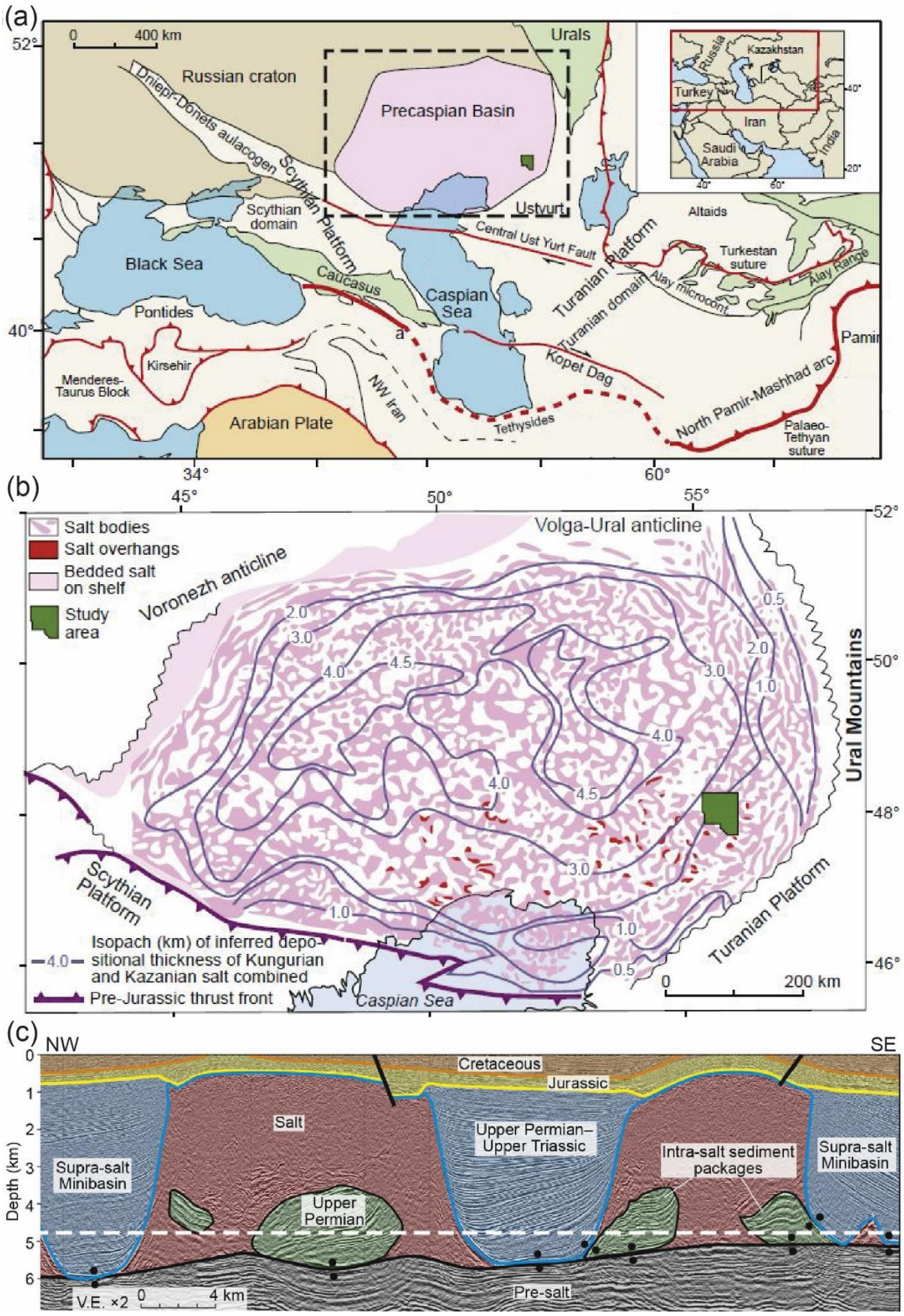

Figure 2 – (a) Regional geological map showing the location and geodynamic context of the Precaspian salt basin (pink). Orogenic belts in green and area in (b) indicated by black dashed lines. (from Duffy et

al., 2017 and after Natal'in and Sengor, 2005). (b) Composite salt thickness and structure map adapted from Volozh et al (2003a) and Duffy et al (2017) showing the location of the 3D survey utilized in this study. (c) Composite seismic section illustrating the main salt tectonic structural elements in the study-area, e.g. large salt walls, encased minibasins and Upper Permian-Upper Triassic supra-salt minibasins, the focus of this study (adapted from Duffy et al., 2017). The minibasins are capped by a major base Jurassic erosional unconformity (BJU) that is represented by a yellow line in the section. For location, see figure 3.

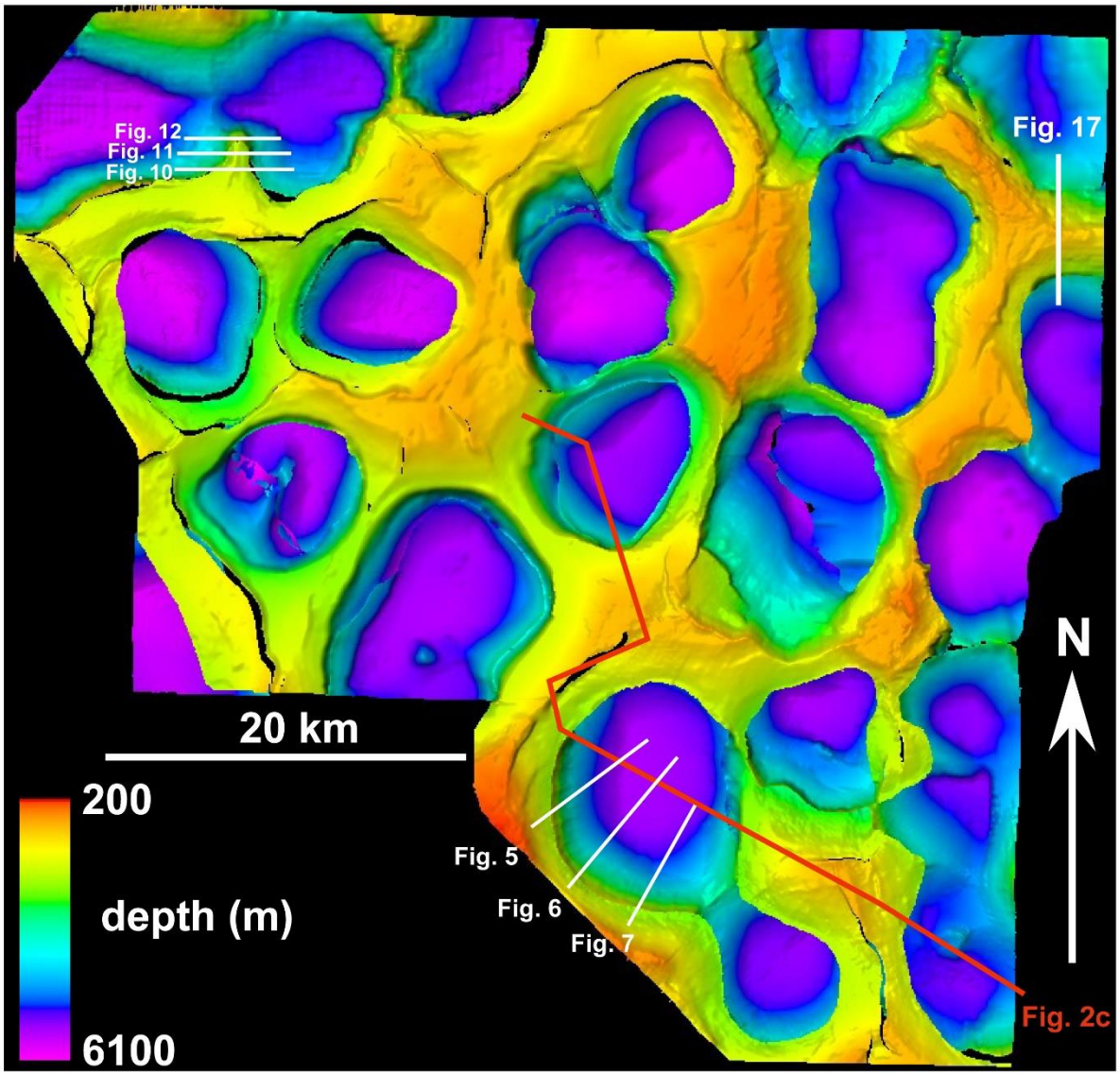

Figure 3: Top Salt Depth-Map illustrating the polygonal structural framework of salt walls and elliptical to sub-circular minibasins in the study-area. The seismic sections presented in this study are indicated in white and another composite section from Duffy et al. (2017) in red.

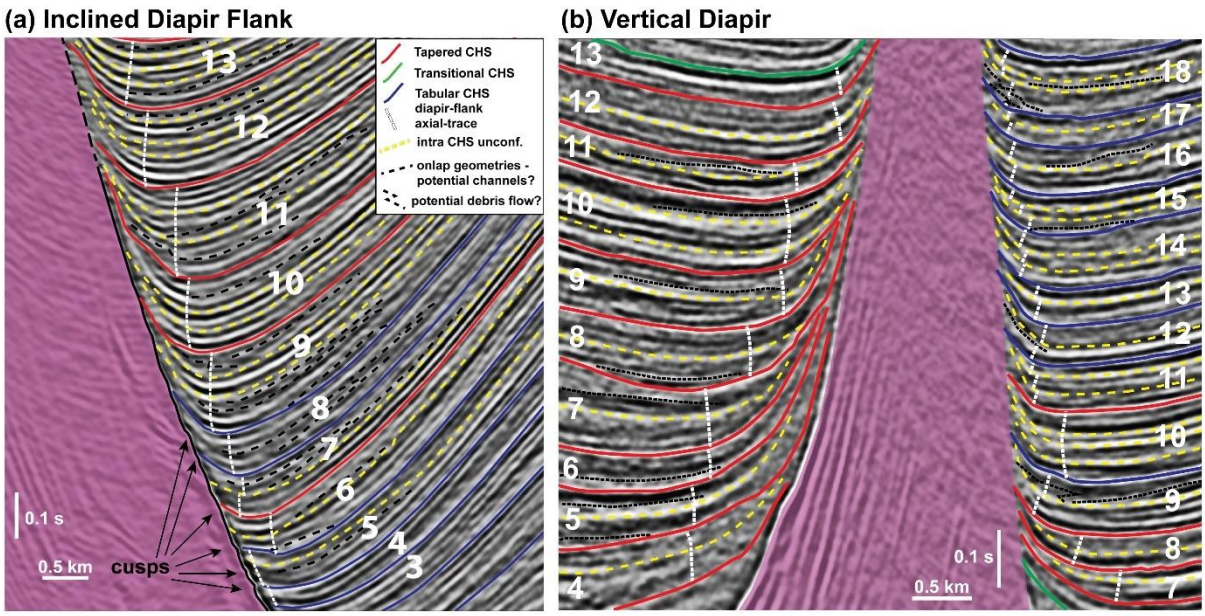

Figure 4: Uninterpreted and Interpreted representative sections showing CHS variability and detailed stratal architecture across two distinct diapir-flank geometries: (a) inclined diapir flank and (b) vertical diapir. Intra-CHS unconformities (yellow dashed lines) relate to 4th order Halokinetic Sequences. Basal onlaps and stratigraphic terminations are indicated in black dashed lines and may potentially indicate channels and debris-flow deposits at/near the depositional axis of CHSs.

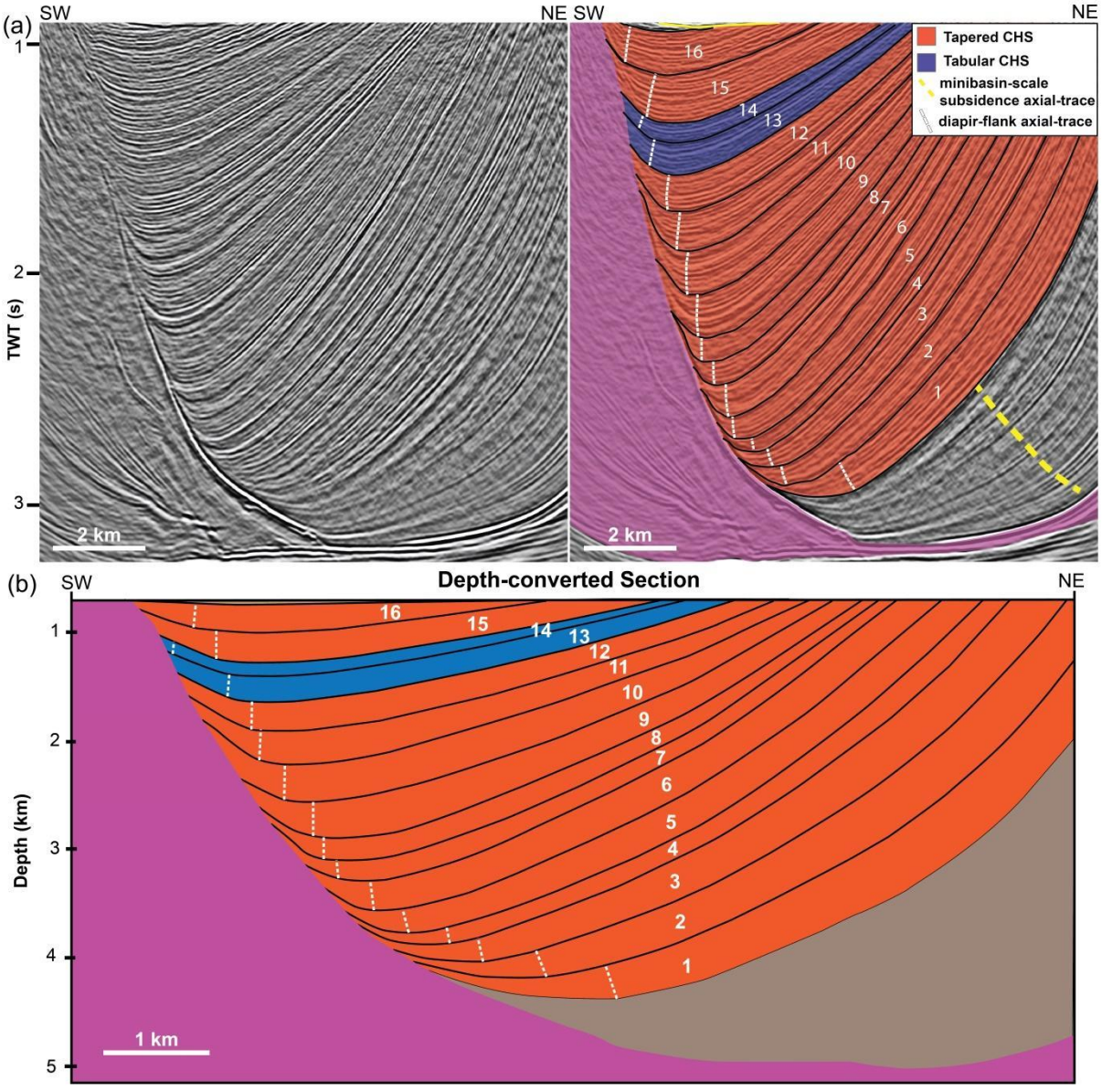

Figure 5: (a) Uninterpreted and interpreted seismic profiles of Section 1 illustrating minibasin and CHS architecture in the northern portion of the inclined salt wall. (c) Depth-converted section. Minibasin strata are tilted to the southwest due to shortening and uplift of a salt wall to the northeast of the section. The lowermost minibasin section (brown) is characterized by a broad, bowl-shape geometry indicating minibasin-scale, broadly symmetric subsidence. This section is overlain by a large-scale wedge sequence composed of a series of CHSs dominated by tapered geometries, i.e. only two tabular CHSs.

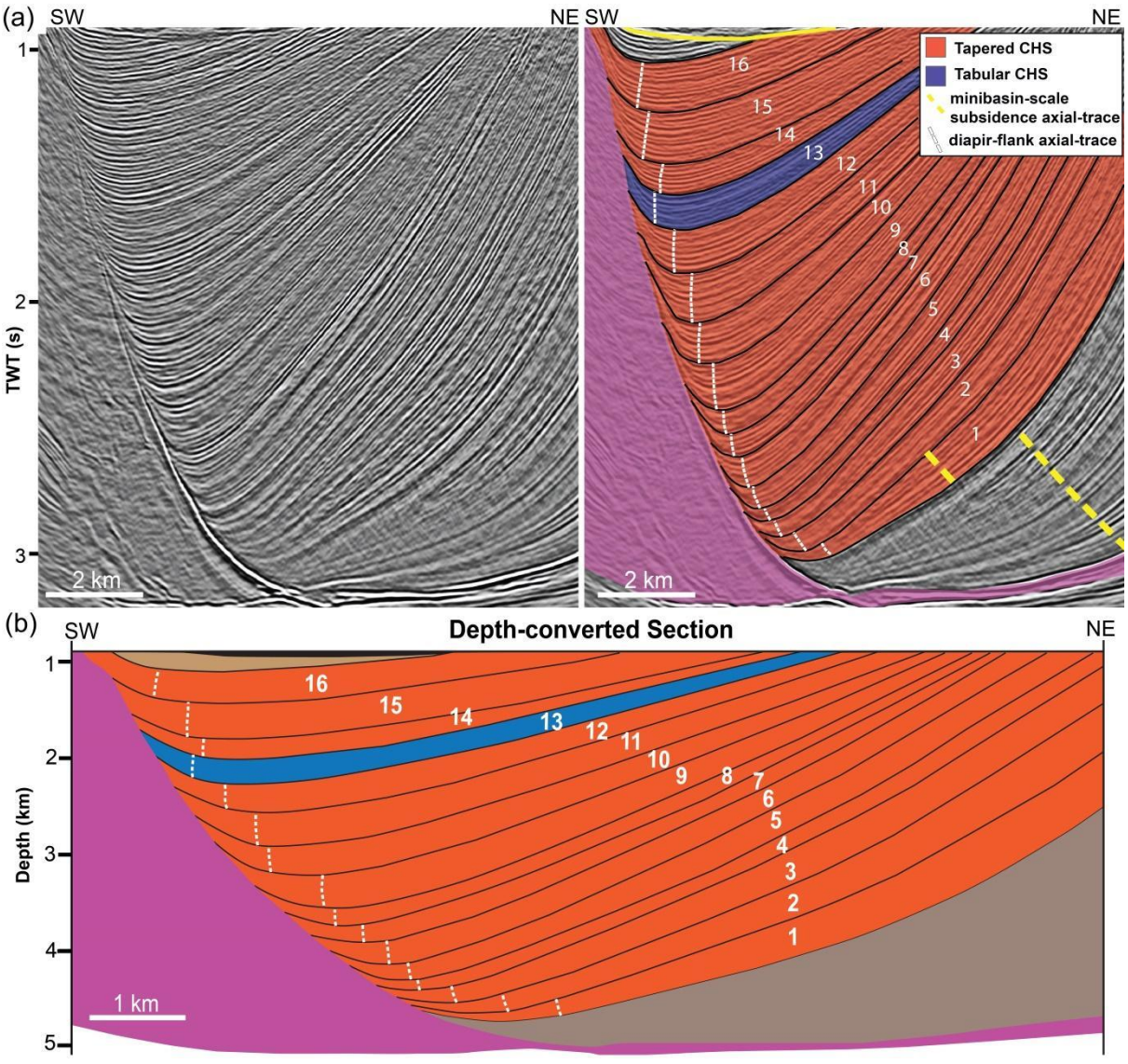

Figure 6: (a) Uninterpreted and interpreted seismic profiles of Section 2 illustrating minibasin and CHS architecture in the central portion of the inclined salt wall. (c) Depth-converted section. Minibasin strata are tilted to the southwest due to shortening and uplift of a salt wall to the northeast of the section. The lowermost minibasin section (brown) is characterized by a broad, bowl-shape geometry indicating minibasin-scale subsidence. This section is overlain by a large-scale wedge succession composed of a series of CHSs dominated by tapered geometries with only one tabular CHS.

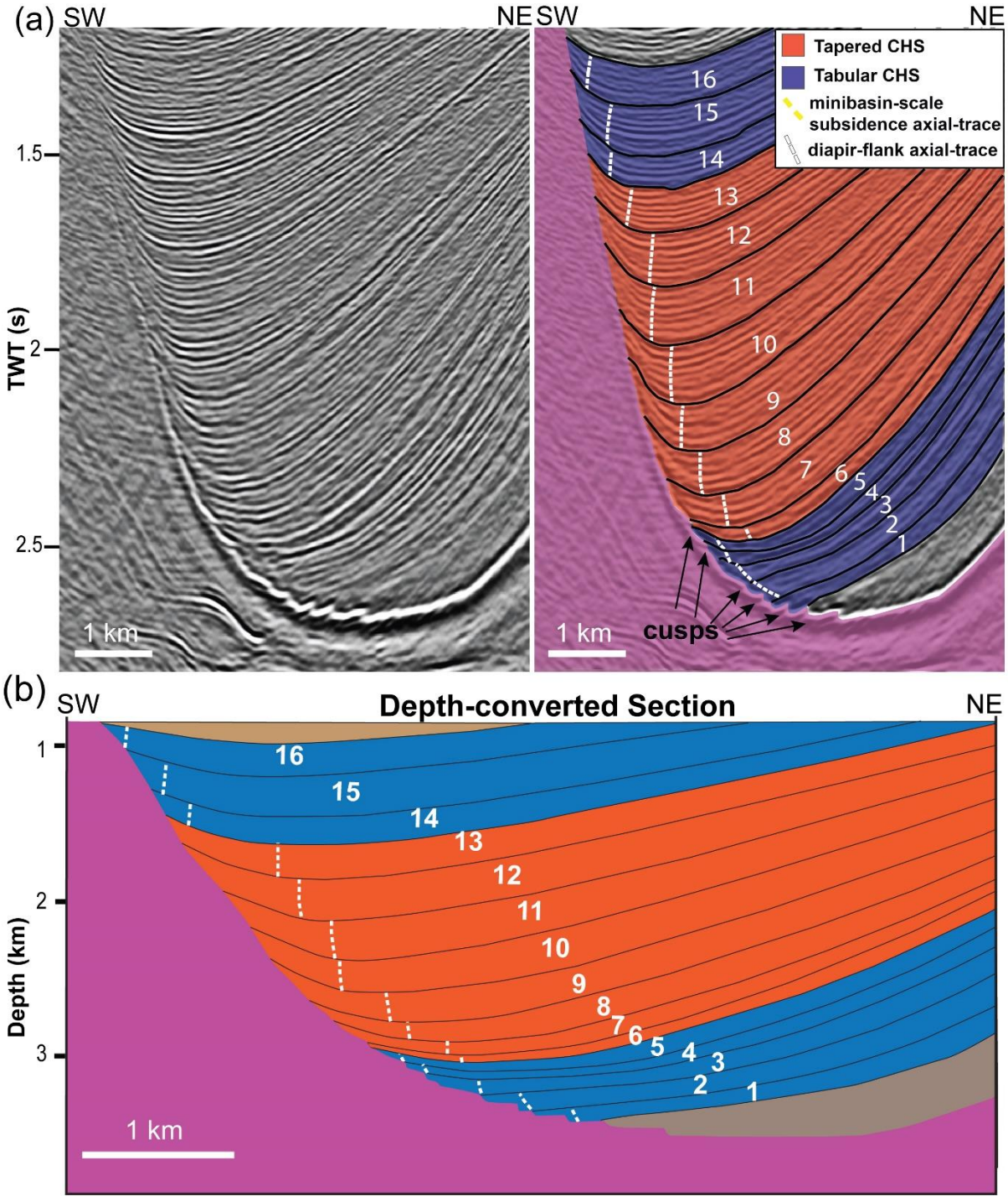

721

722 *Figure 7: (a) Uninterpreted and interpreted seismic profiles of Section 3 illustrating minibasin and CHS*
723 *architecture in the northern portion of the inclined salt wall. (c) Depth-converted section. Minibasin strata*
724 *are tilted to the southwest due to shortening and uplift of a salt wall to the northeast of the section.*
725 *Lower and uppermost undifferentiated sequences in brown and CHSs in blue and red according to their*
726 *end-member geometries. The succession shows an equal proportion of tabular (blue) and tapered (red)*
727 *end-members and an atypical vertical zonation characterized by lower and upper tabular CHSs and*

intermediate tapered CHSs. Prominent cusps occur where bounding unconformities of lowermost CHSs intersect the salt-sediment interface.

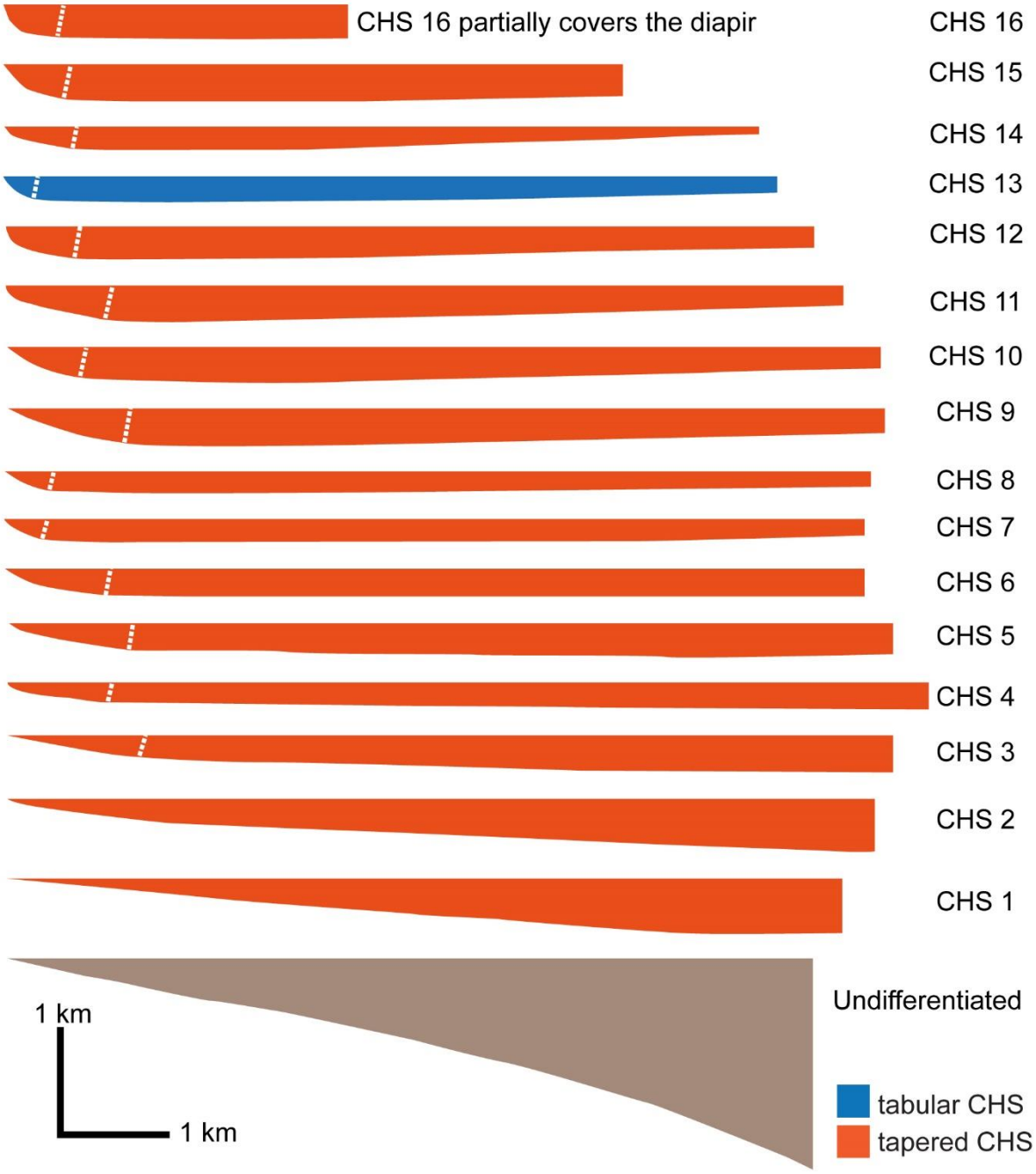

Figure 8: Central section (Section 2) analysis demonstrating the restored geometry and classification for each CHS identified. Dashed white lines represent the restored depositional axial traces associated with monoclinal drape folding characteristic of the CHS development. In many CHSs, especially oldest CHSs, the influence of broader-scale minibasin subsidence produce very subtle, low-amplitude and high wavelength stratal thinning, which hinders the definition of CHSs 1-2 axial trace.

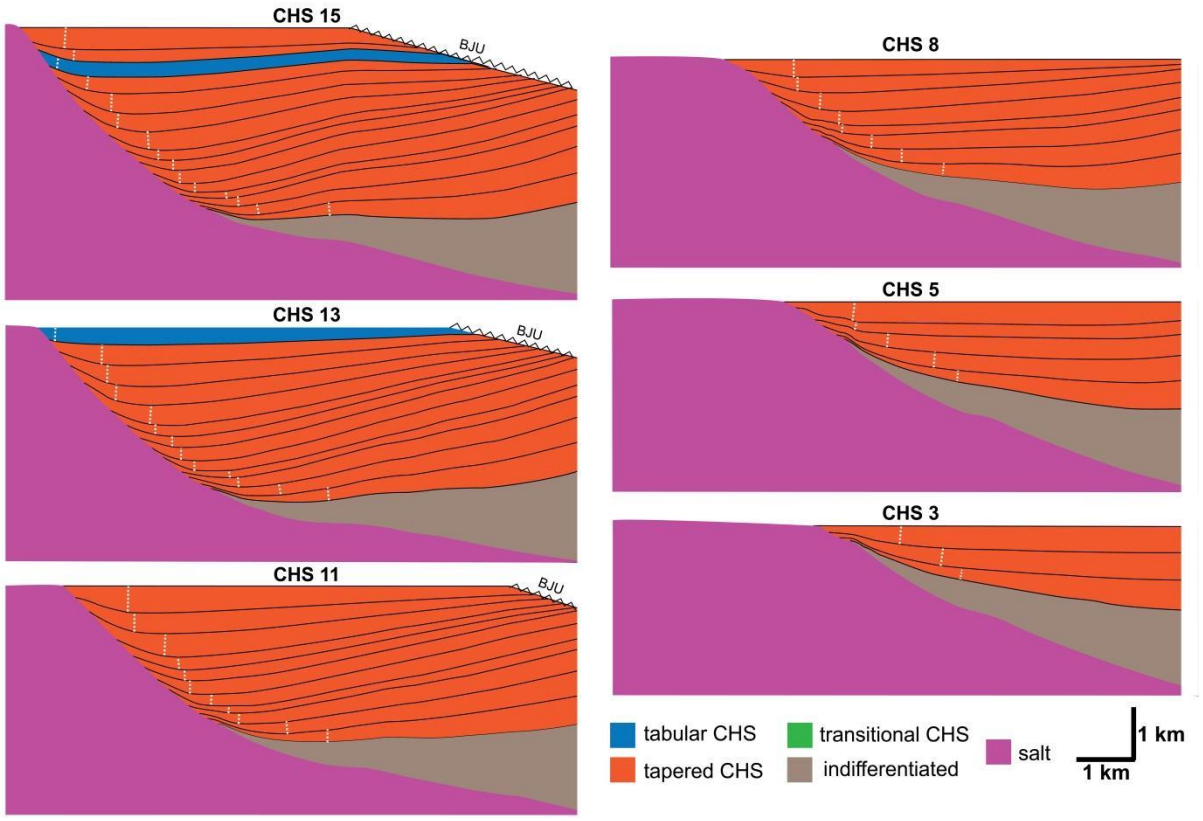

736

737 *Figure 9: Sequential restoration of the central section (Section 2) showing the main, most representative*
738 *steps of minibasin subsidence, development of CHS and their relationship with changes in diapir-flank*
739 *geometries associated with the inclined salt wall. BJU is the Base-Jurassic Unconformity. The white-*
740 *dashed lines represent restored CHS axial-traces.*

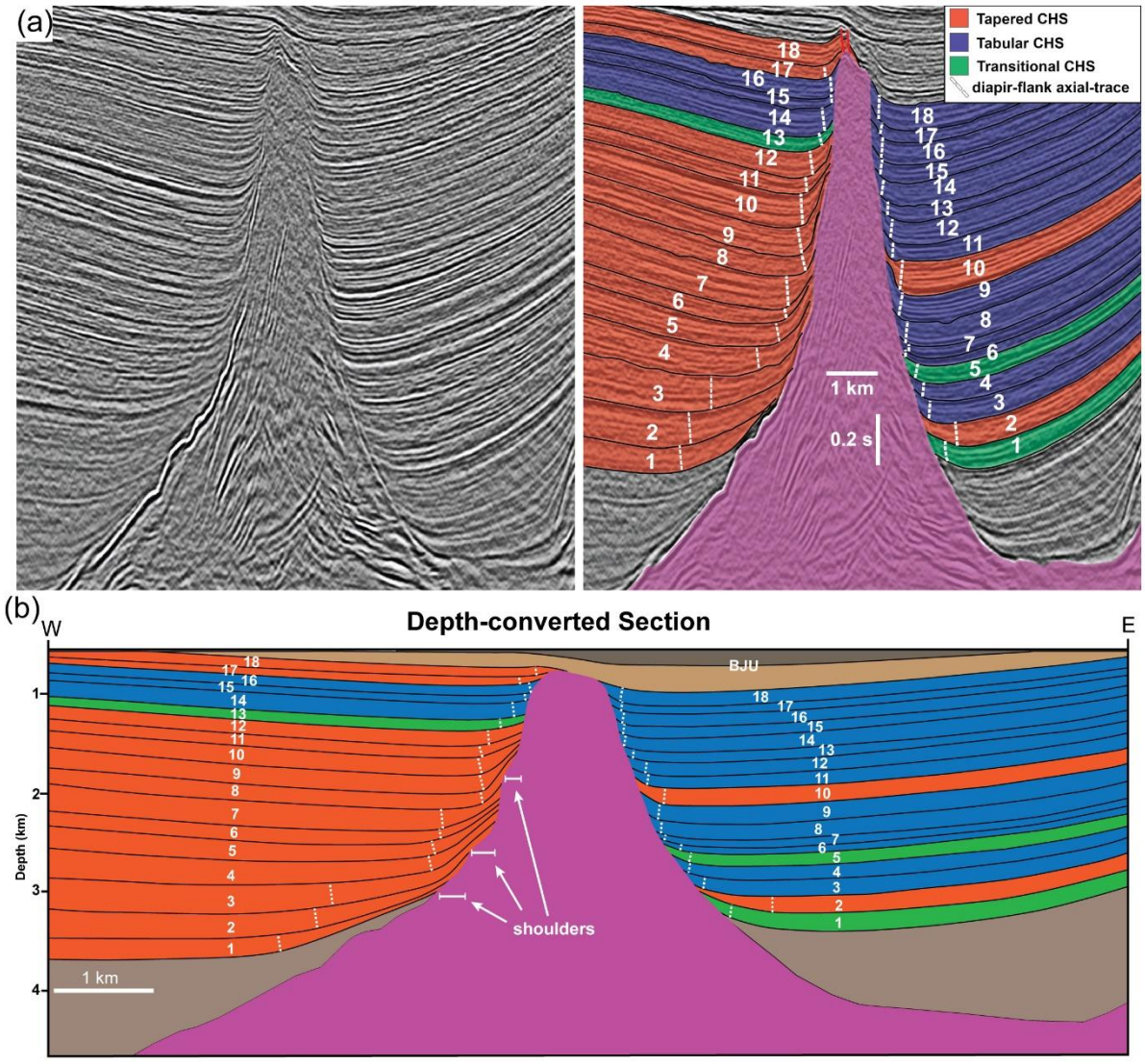

741

742 *Figure 10: (a) Uninterpreted and interpreted seismic profiles of Section 1 illustrating minibasin and CHS*
743 *architecture and variability along the southern portion of the vertical salt wall. (b) Depth-converted*
744 *section. These sections show how the large majority of CHSs change laterally to different CHS end-*
745 *members along-strike and around the vertical diapir. The western minibasin is dominated by tapered*
746 *end-members whereas the eastern by tabular end-members. The lowermost minibasin section (brown)*
747 *is characterized by a broad, bowl-shape geometry indicating minibasin-scale, broadly symmetric*
748 *subsidence. Uppermost section (light brown) is undifferentiated as it partially covers the diapir and do*
749 *not present CHSs. BJU is Base-Jurassic Unconformity.*

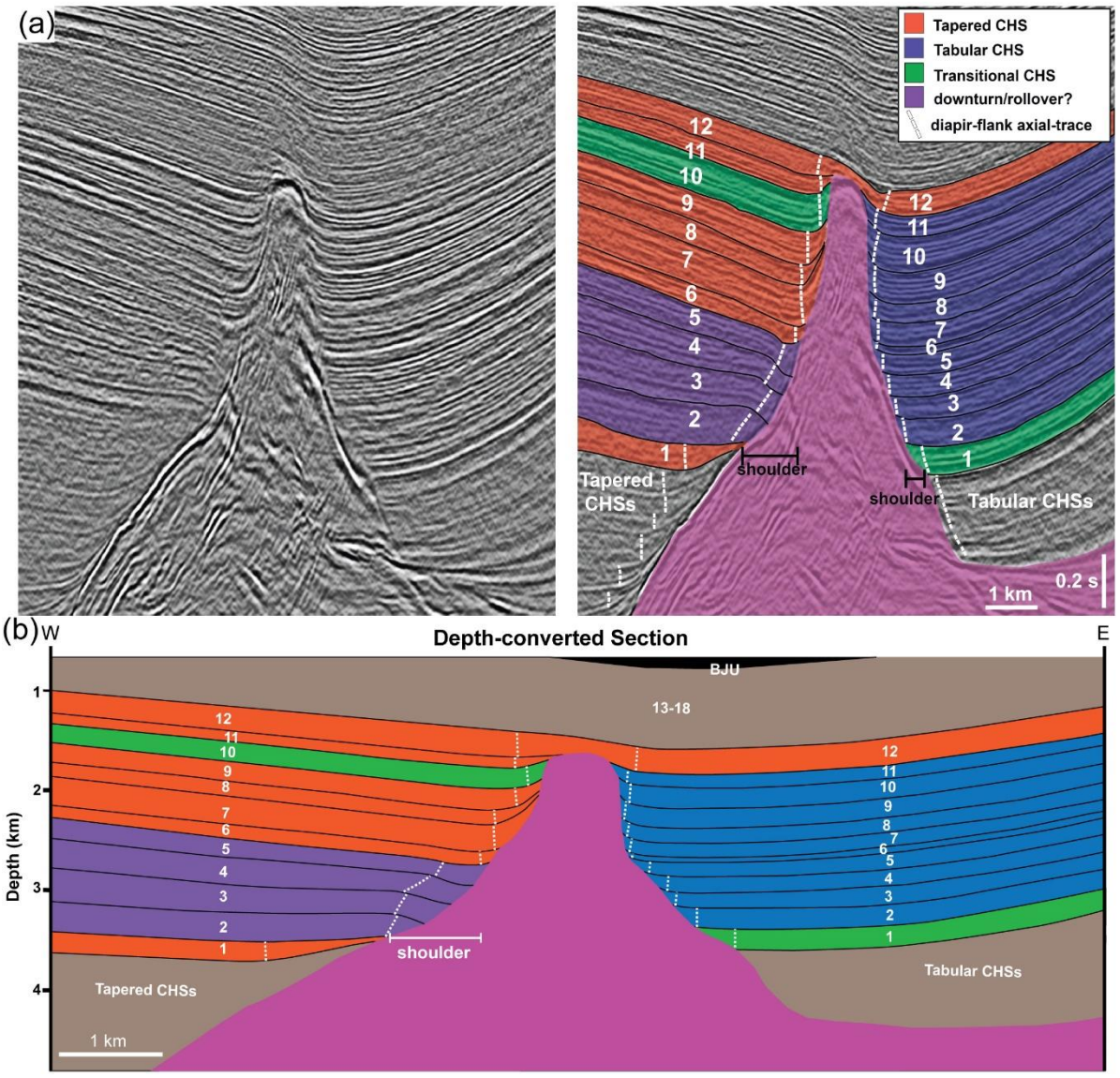

Figure 11: (a) Uninterpreted and interpreted seismic profiles of Section 2 illustrating minibasin and CHS architecture and variability along the central portion of the vertical salt wall. (b) Depth-converted section. Illustrating drastic variability of CHS style across the vertical salt wall, with the eastern minibasin dominated by tabular CHSs and the western minibasin by tapered CHSs. The eastern minibasin presents intermediate sequences with rollover geometries characterized by downturning and thickening towards the diapir above a salt shoulder. The lowermost minibasin section is not numbered but is characterized by tabular CHSs geometries to the east and tapered geometries to the west. The upper section (light brown) is equivalent to the CHSs 13-18 from further south (section 1) but, here, as they cover the diapir, they are not classified as CHSs and, thus, are undifferentiated. BJU is Base-Jurassic Unconformity.

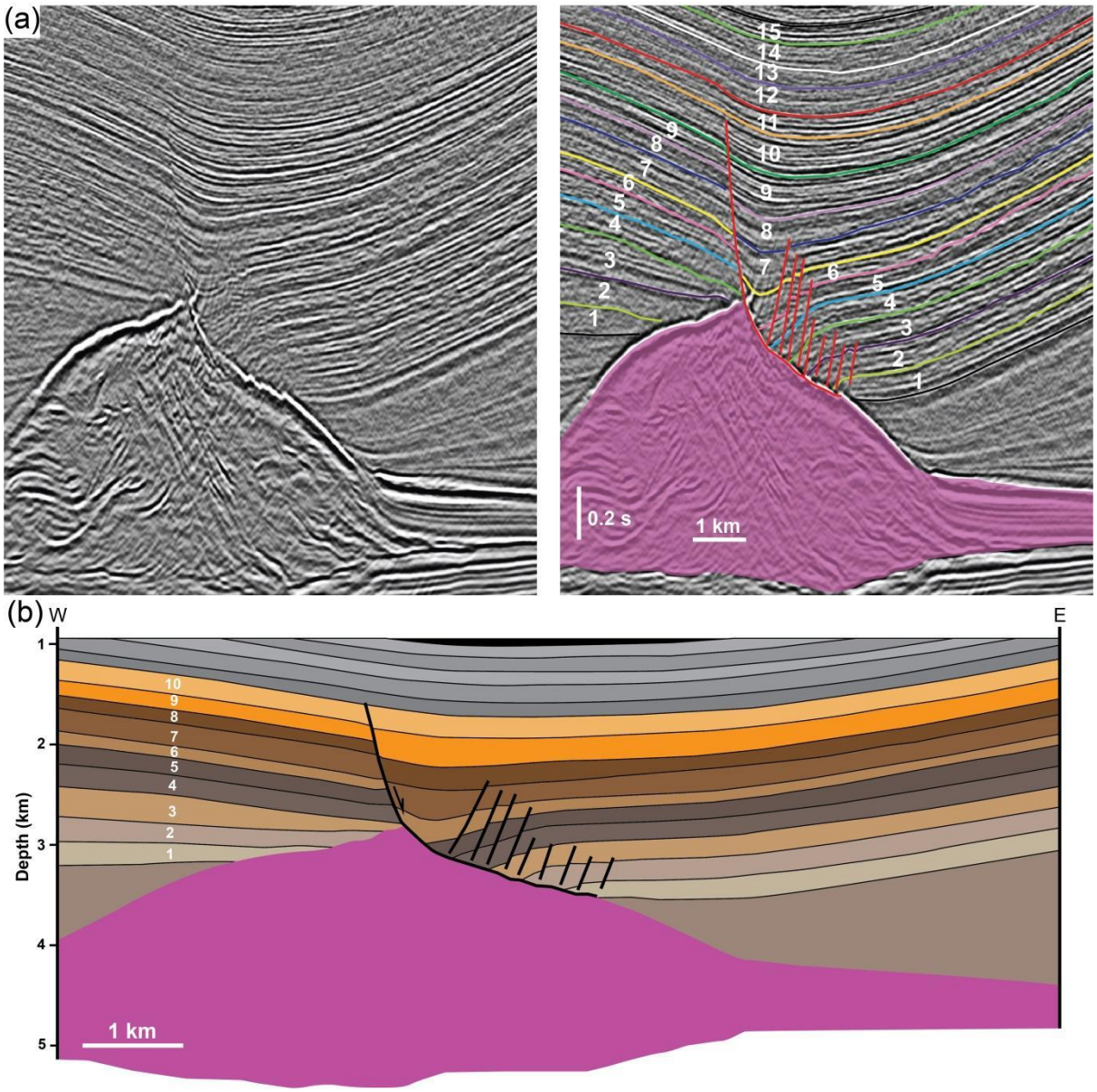

Figure 12: (a) Uninterpreted and interpreted seismic profiles of Section 3, and (b) depth-converted section showing how the salt wall changes to the north to a low-relief salt roller defined by a listric normal fault and a west-dipping extensional rollover. Sequences 1-10 (warm colours) demonstrate rollover and/or hanging-wall thickening geometries denoting syn-extension deposition. Strata equivalent to CHSs further south are no longer classified as CHSs as they are controlled and deformed by the listric normal fault, not being associated with passive diapirism.

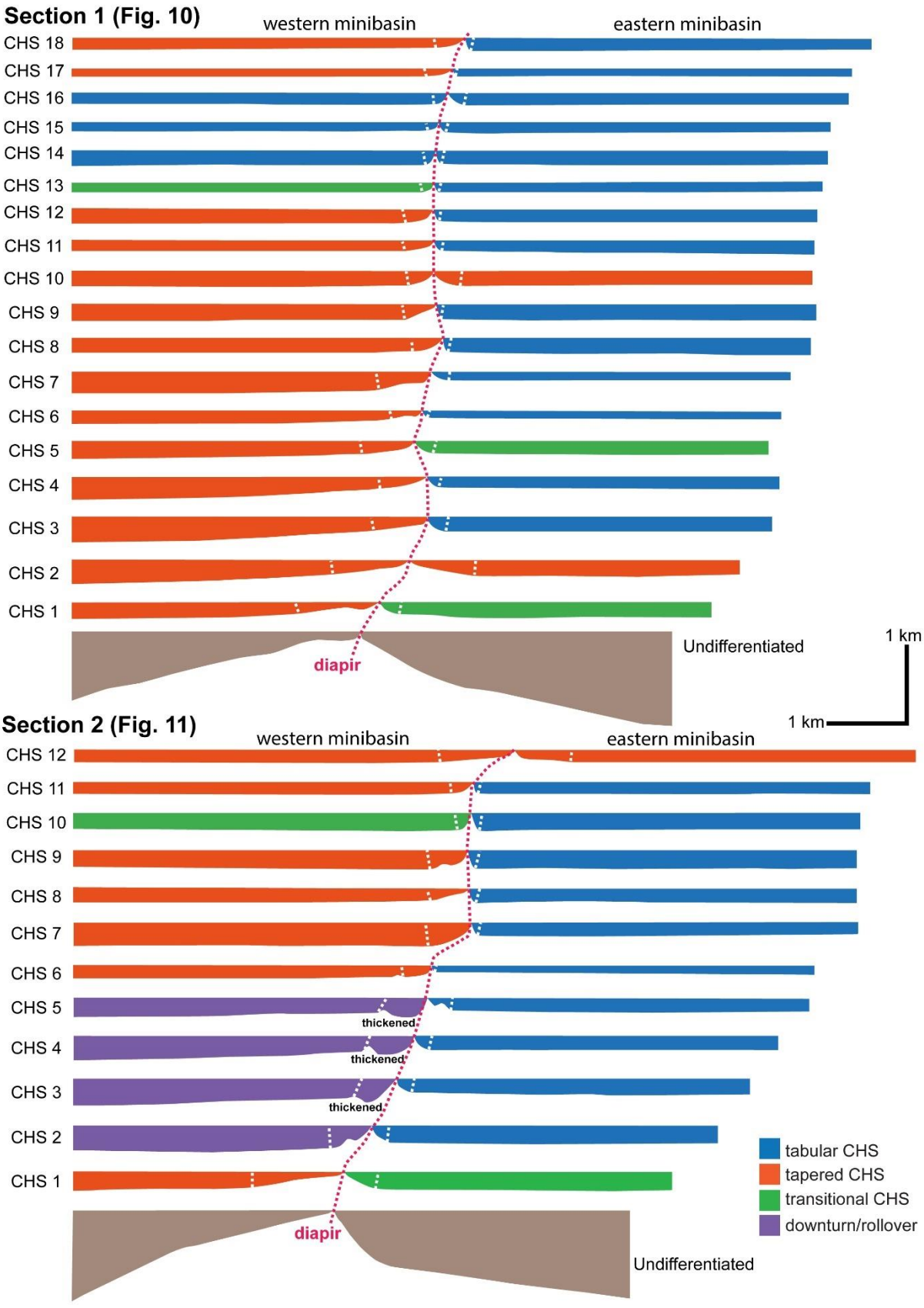

769

770 *Figure 13: Section analysis for (a) Section 1 (south) and (b) Section 2 (central) demonstrating the*

771 *restored geometry and classification for each CHS on both western and eastern minibasins around the*

vertical diapir. Dashed white lines represent the restored depositional axial traces associated with monoclinal drape folding characteristic of the CHS development. The pink-dashed line indicates the diapir-margin limit of each individual CHS.

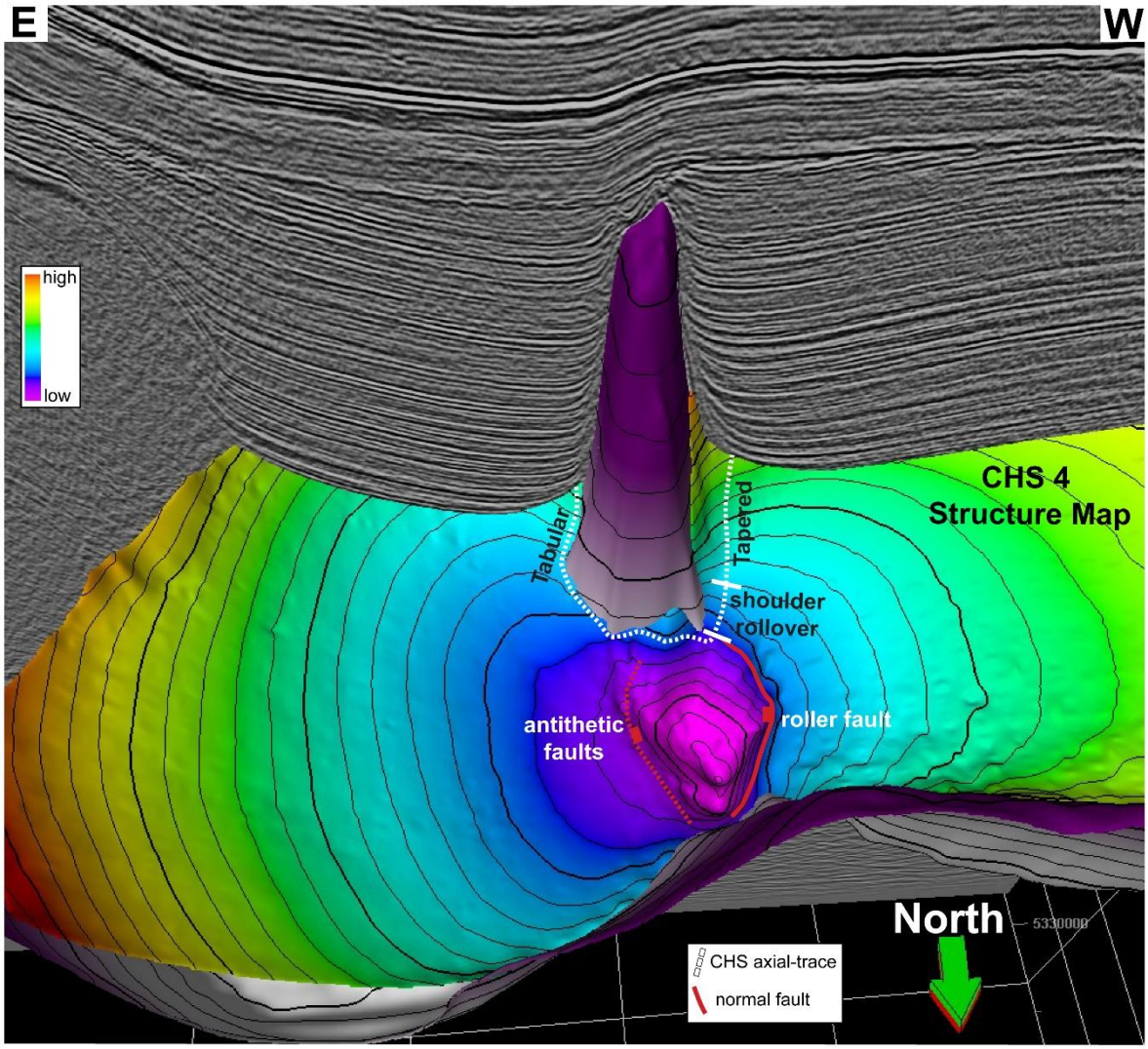

Figure 14: 3D view of the vertical salt wall combined to the CHS 4 structure map demonstrating how CHS architecture changes along-strike and around the wall from tabular CHS geometries to the east and north of the wall to an intermediate rollover above a salt shoulder to the northwest and to tapered CHS geometries to the west. Away from the vertical salt wall, CHS 4 is affected by listric normal faults associated with a salt roller.

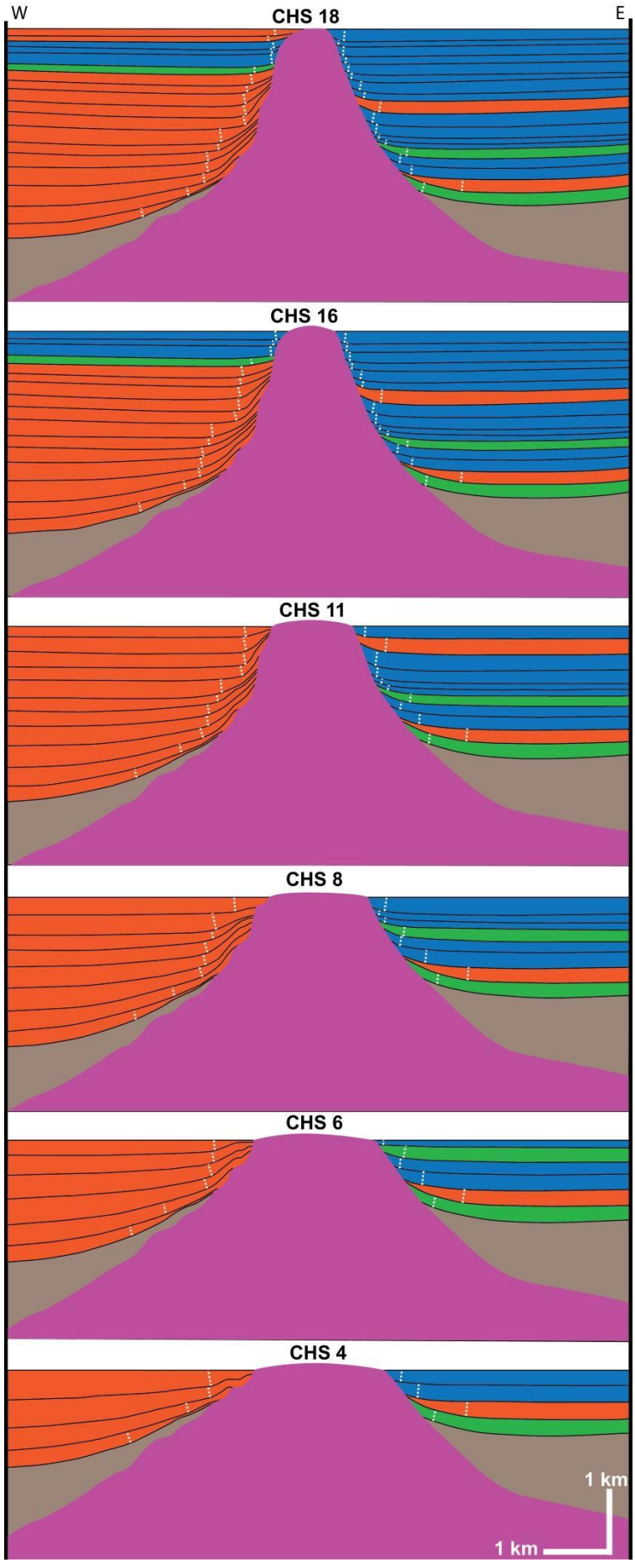

781

Figure 15: Sequential restoration of the southern section (Section 1, figure 10) of the vertical salt wall showing the most representative steps of development of CHS and their relationship with changes in diapir geometries. BJU is Base-Jurassic Unconformity. The white-dashed lines represent restored CHS axial-traces. For the colour classification scheme and figure caption, see figure 9 and 16.

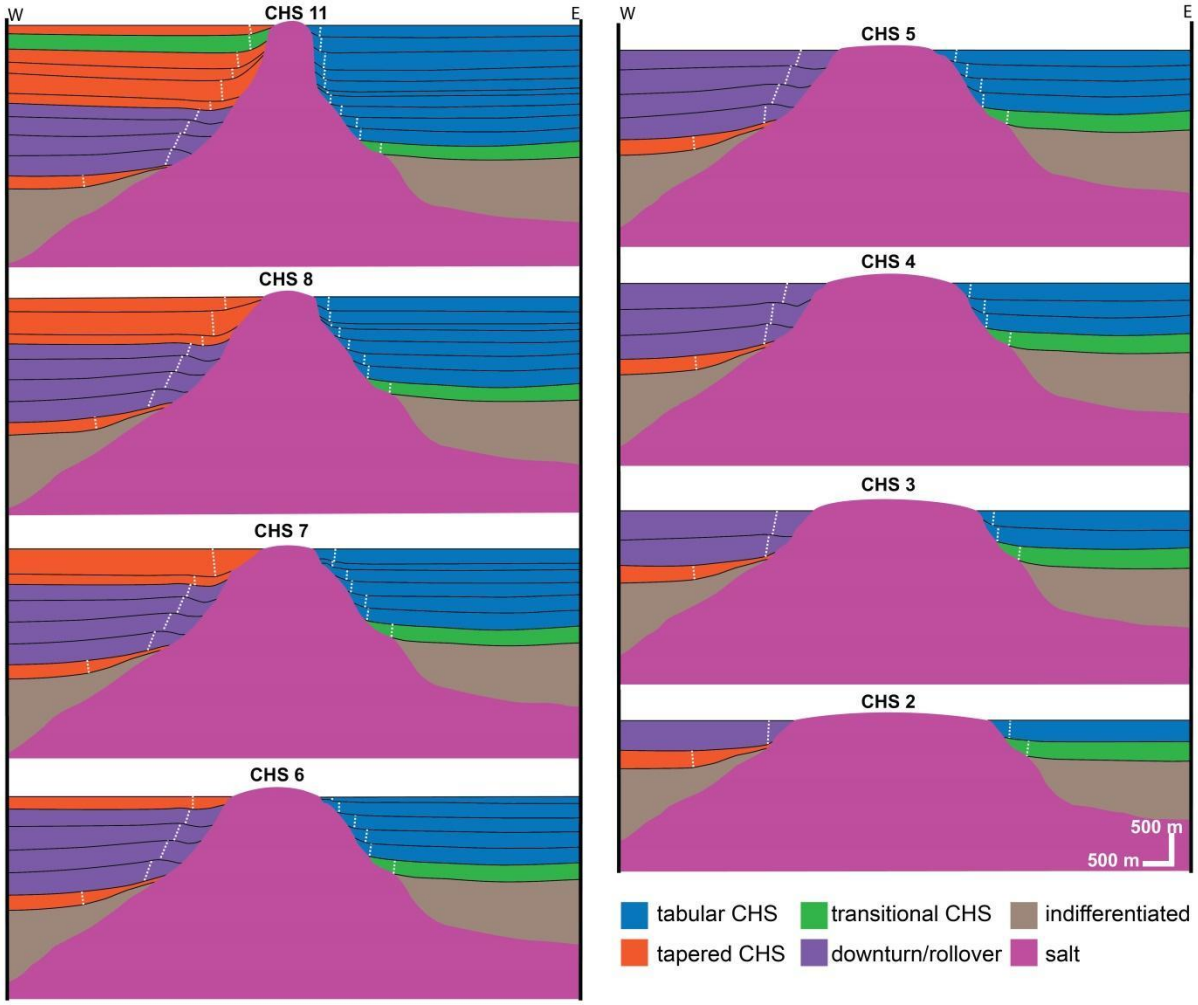

Figure 16: Sequential restoration of the central section (Section 2, figure 11) of the vertical salt wall showing the most representative steps of development of CHS and their relationship with diapir geometries. BJU is Base-Jurassic Unconformity. The white-dashed lines represent restored CHS axial-traces.

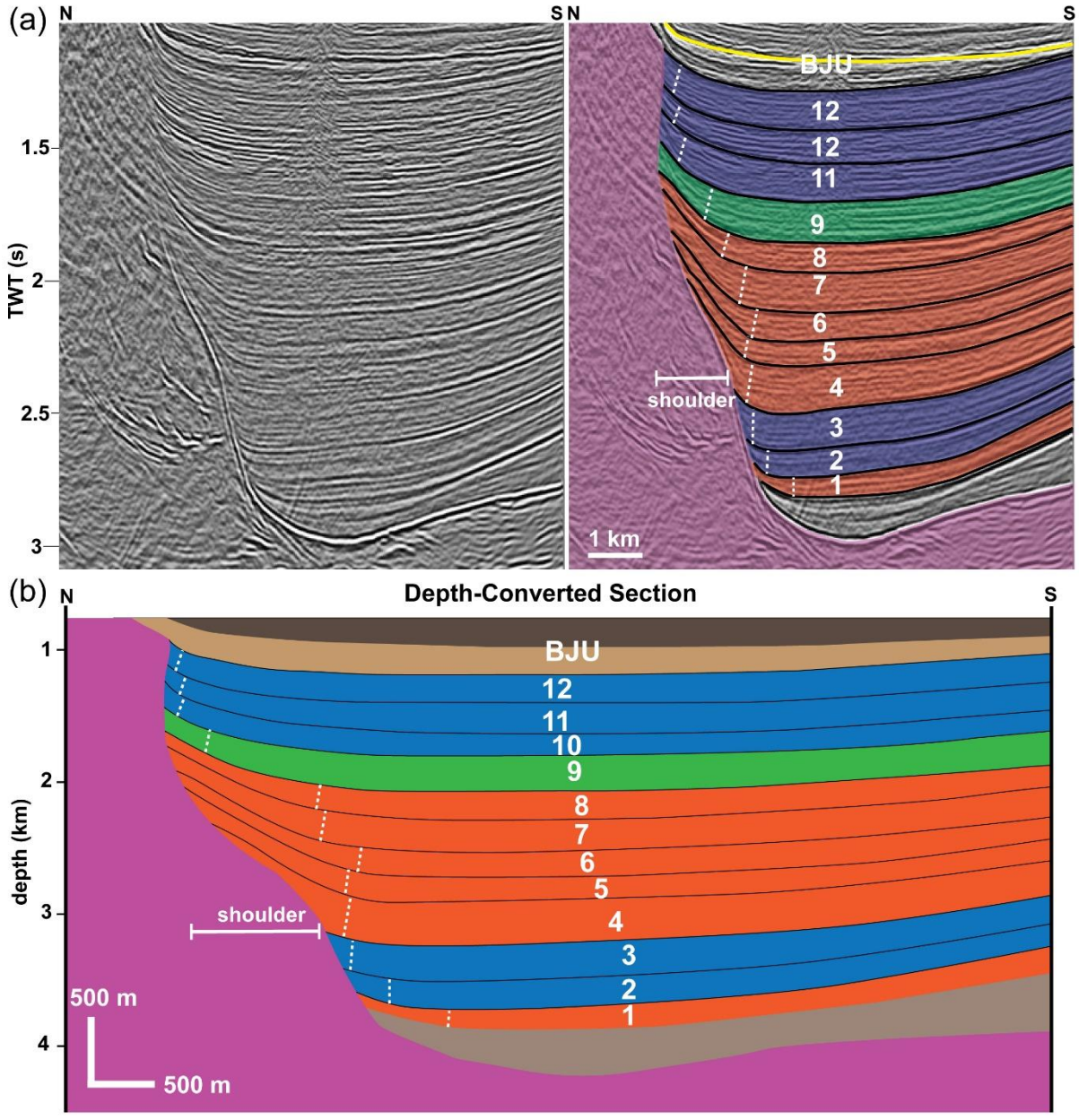

Figure 17: (a) uninterpreted and interpreted seismic sections illustrating a CHS succession from a different minibasin in the north of the study-area and the transition from pre-shoulder tabular CHSs to tapered geometries with significantly wider (c. 500 m) zone of folding and stratal thinning over the shoulder. White dashed lines indicate CHS axial-trace. (c) Depth-converted section. Yellow line indicates the BJU, Base-Jurassic Unconformity. For colour scheme and classification, see figures 10 and 16.

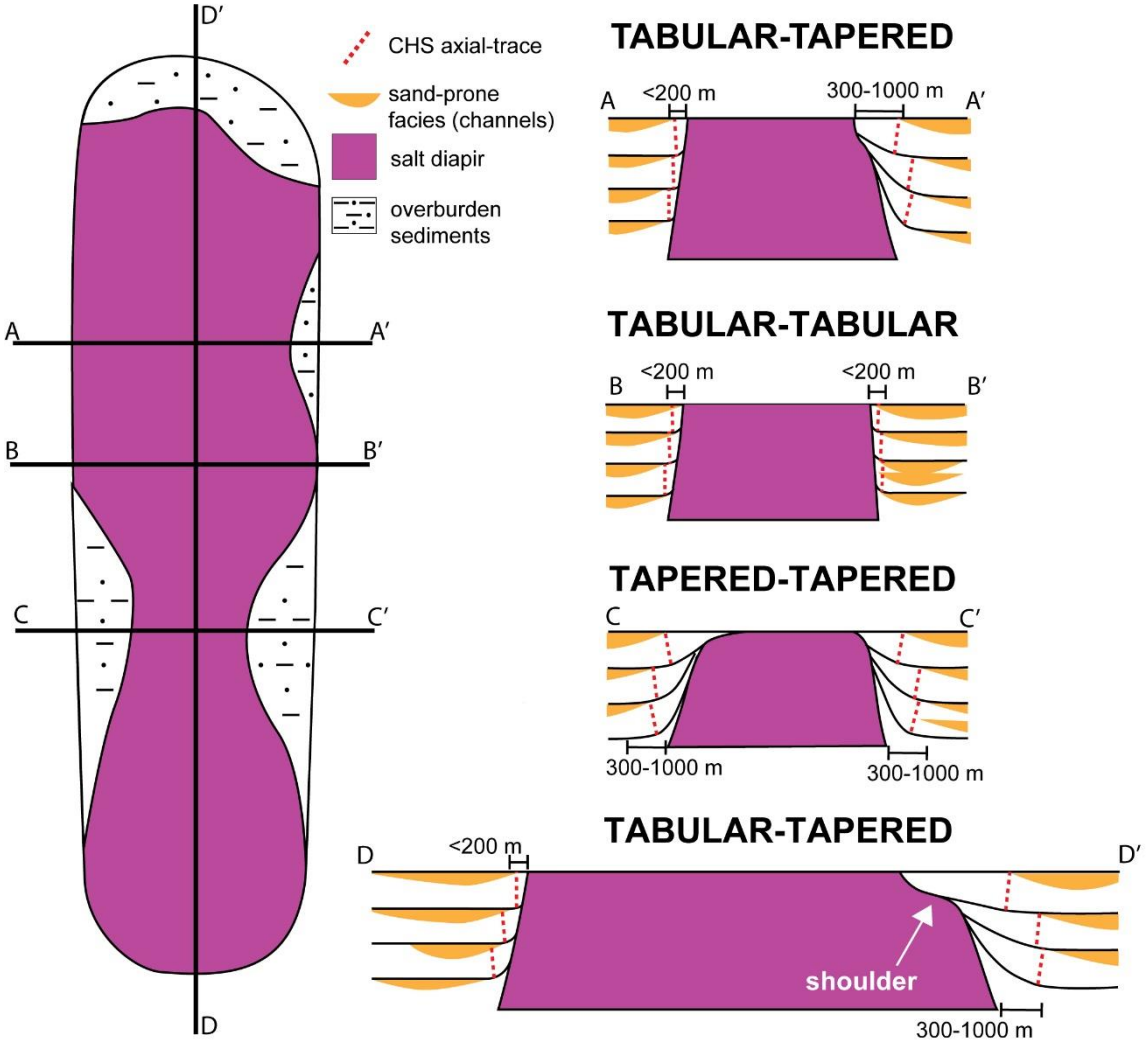

798

799 *Figure 18: Diagram summarizing how diapir-flank and CHS geometries can vary three-dimensionally*
800 *and how this is influenced by how further inboard the cover the diapir, which is turn a consequence of*
801 *volumetrically variable salt flux and sediment accumulation rate. They present variable geometries and,*
802 *in cases, contrasting end-members along a single diapir. This may result in laterally variable distribution*
803 *of sand-prone facies in clastic-dominated systems and, ultimately on diapir-flank reservoir pinch-out.*
804 *Tabular geometries will have updip pinch-outs located up to 200 m from the salt-sediment interface*
805 *whereas in tapered geometries this distance will range from 300-1000 m.*

806

807

808

809

810

TABLES

Inclined Wall												
Section 1 (Northern)				Section 2 (Central)						Section 3 (Southern)			
	Depth-Converted				Depth-Converted		Restored				Depth-Converted		
	Taper Angle	Width of Thinning/Folding zone (m)	CHS type		Taper Angle	Width of Thinning/Folding zone	Taper Angle	Width of Thinning/Folding zone (m)	CHS type		Taper Angle	Width of Thinning/Folding zone (m)	CHS type
CHS16	-	-	Tapered	CHS16	-	-	22	540	Tapered	CHS16	-	-	Tapered
CHS15	30	690	Tapered	CHS15	45	390	32	450	Tapered	CHS15	40	390	Tapered
CHS14	64	90	Tabular	CHS14	33	550	19	630	Tapered	CHS14	60	100	Tabular
CHS13	62	130	Tabular	CHS13	60	170	54	190	Tabular	CHS13	34	470	Tapered
CHS12	32	750	Tapered	CHS12	38	580	23	770	Tapered	CHS12	44	360	Tapered
CHS11	34	750	Tapered	CHS11	33	800	21	950	Tapered	CHS11	33	590	Tapered
CHS10	37	860	Tapered	CHS10	37	690	26	640	Tapered	CHS10	34	560	Tapered
CHS9	30	880	Tapered	CHS9	32	860	22	970	Tapered	CHS9	22	800	Tapered
CHS8	35	645	Tapered	CHS8	26	610	17	690	Tapered	CHS8	12	870	Tapered
CHS 7	31	790	Tapered	CHS 7	16	850	15	950	Tapered	CHS 7	10	930	Tapered
CHS6	28	730	Tapered	CHS6	22	745	20	840	Tapered	CHS6	8	860	Tapered
CHS5	26	900	Tapered	CHS5	18	860	16	980	Tapered	CHS5	8	900	Tapered
CHS4	16	940	Tapered	CHS4	20	640	11	850	Tapered	CHS4	-	140	Tabular
CHS3	13	1250	Tapered	CHS3	11	900	14	975	Tapered	CHS3	-	130	Tabular
CHS2	11	1350	Tapered	CHS2	5	1320	12	1450	MB-scale	CHS2	-	185	Tabular
CHS1	10	2100	MB-scale	CHS1	-	-	7	~ 4500	MB-scale	CHS1	-	175	Tabular

Table 1: Classification and metrics of each CHS mapped in the sections (1-3) for the inclined salt wall. Measurements were obtained from depth-converted sections. For the central section we compare these values for both present-day and restored geometries. The widths of folding were measured from the inflection points to the tips of each CHS and taper angles by straight lines connecting these two points.

Vertical Wall Section 1									
Restored		Depth-Converted		CLASSIFICATION			Depth-Converted		Restored	
Taper Angle	Width of Thinning/Folding zone	Taper Angle	Width of Thinning/Folding zone	LEFT MB		RIGHT MB	Taper Angle	Width of Thinning/Folding zone	Taper Angle	Width of Thinning/Folding zone
15	370	13	440	Tapered	CHS18	Tabular	46	190	41	170
12	400	16	460	Tapered	CHS17	Tabular	40	152	36	135
53	150	56	190	Tabular	CHS16	Tabular	71	62	68	75
72	30	72	45	Tabular	CHS15	Tabular	56	83	53	88
62	100	74	40	Tabular	CHS14	Tabular	70	50	60	95
40	280	43	240	Transitional	CHS13	Tabular	65	54	64	60
34	355	38	310	Tapered	CHS12	Tabular	51	118	49	140
18	460	21	410	Tapered	CHS11	Tabular	50	114	46	126
21	350	35	370	Tapered	CHS10	Tapered	26	300	18	310
30	420	49	380	Tapered	CHS9	Tabular	68	105	60	140
22	500	48	420	Tapered	CHS8	Tabular	66	73	61	120
21	850	28	620	Tapered	CHS 7	Tabular	63	45	62	45
20	550	32	550	Tapered	CHS6	Tabular	49	52	40	95
16	790	38	680	Tapered	CHS5	Transitional	33	220	29	270
19	620	38	730	Tapered	CHS4	Tabular	52	120	45	150
14	1070	18	1630	Tapered	CHS3	Tabular	53	130	50	145
13	1100	17	1820	Tapered	CHS2	Tapered	18	810	17	915
11	1180	17	1970	"Tapered"	CHS1	Transitional	44	215	33	270

Table 2: Classification and metrics of the present-day and restored geometries of each CHS mapped in the south section of the vertical salt wall (figure 10). Measurements were obtained from depth-converted sections. The widths of folding were measured from the inflection points to the tips of each CHS and taper angles by straight lines connecting these two points.

Vertical Wall Section 2						
		CLASSIFICATION			Depth-Converted	
Taper Angle	Width of Thinning/Folding zone	LEFT MB		RIGHT MB	Taper Angle	Width of Thinning/Folding zone
-	-	-	CHS18	-	-	-
-	-	-	CHS17	-	-	-
-	-	-	CHS16	-	-	-
-	-	-	CHS15	-	-	-
-	-	-	CHS14	-	-	-
-	-	-	CHS13	-	-	-
-	470	Tapered	CHS12	Tapered	-	340
21	325	Tapered	CHS11	Tabular	67	87
38	240	Transitional	CHS10	Tabular	86	25
42	350	Tapered	CHS9	Tabular	82	36
33	470	Tapered	CHS8	Tabular	84	20
49	450	Tapered	CHS 7	Tabular	77	45
16	420	"Tapered"	CHS6	Tabular	80	20
-	540	Downturn/RV	CHS5	Tabular	46	200 (transition to shoulder)
-	680	Downturn/RV	CHS4	Tabular	54	130
-	520	Downturn/RV	CHS3	Tabular	53	90
-	370	Downturn/RV	CHS2	Tabular	47	160
11	1100	Tapered	CHS1	Transitional	29	295 (transition to shoulder

Table 3: Classification and metrics of the present-day and restored geometries of each CHS mapped in the central section of the vertical salt wall (figure 11). Measurements were obtained from depth-converted sections. The widths of folding were measured from the inflection points to the tips of each CHS and taper angles by straight lines connecting these two points. CHSs 2-5 present distinct downturned and thickened strata in the western minibasin and, thus, are classified as rollover (RV) sequences. Sequences 13-18, defined as CHS further south (Section 1), are not classified as such here as they cover the diapir and, therefore, do not present typical CHS folding and thinning strata.